SPIN-DEPENDENT TRANSPORT IN NANOSCALE STRUCTURES

A Dissertation

Presented to the Faculty of the Graduate School

of Cornell University

in Partial Fulfillment of the Requirements for the Degree of

Doctor of Philosophy

by

Kirill I. Bolotin

January 2007

This document is in the public domain.

SPIN-DEPENDENT TRANSPORT IN NANOSCALE STRUCTURES

Kirill I. Bolotin, Ph.D.

Cornell University 2007

If a metallic particle is sufficiently small (< 15 nm), its discrete spectrum of "electron in a box" states can be resolved by tunnel spectroscopy at low temperatures. We will first discuss a technique that introduces several previously unavailable "knobs" to study the quantum states of an individual nanoparticle: we can control the number of electrons on the particle by using efficient gate electrodes, and the size and composition of the particle using chemical synthesis. In gold nanoparticles we find that quantum states are spin-degenerate and are filled as in a non-interacting model, consistent with weak exchange interactions. The second part of the thesis focuses on developing ferromagnetic contacts to study spin-dependent transport through the nanoparticle. We discuss a technique which allows us to fabricate such contacts with tunable size down to the atomic scale and into the tunneling regime, and to study spin transport in atomically-narrow contacts. We find a large anistropic magnetoresistance contribution in such contacts and interpret it as a consequence of mesoscopic quantum interference.

BIOGRAPHICAL SKETCH

Kirill Igorevich Bolotin was born in Moscow, Russia in 1978. After attending several schools further and further away from his home, he finally found the fartherst one (School N1543, one-hour long subway ride away). After almost failing the chemistry class, he somehow graduated in 1994. He then joined the physics program in Moscow Institute of Physics and Techology. After several years in college he found an adviser working on quantum gravity and decided only to study systems larger than galaxies. In the year 2000, he introduced several small corrections to this course: he decided to switch from theory to experiments, length scale from large to small, and the country from Russia to America and joined Dan Ralph's group at Cornell. Six years down the road, Kirill is happily mixing chemicals in the lab and takes prides in his soldering. His next stop is Columbia University, where he will work in the Philip Kim and Horst Stormer groups.

ACKNOWLEDGEMENTS

I would like to thank all the friends and colleagues who made these six years in Ithaca enjoyable and productive.

I am most grateful to my advisor, Dan Ralph, for all the support and patience over the years. Dan, from my day one when you taught me soldering the right way^{TM} you were the best boss one can ask for. Thanks to you, I had all the helium and equipment I could ask for, all the freedom to explore the ideas I liked and all the advice when I needed it. I now understand how one can preserve his scientific integrity, follow what is important not what is fashionable, stay humble, and yet remain on top of his field.

Experiments are a team effort, and I was lucky to be a member of the best team in town. Ralph group, you were my family for the last six years, and I would like to thank both elder and younger brothers and sisters.

Mandar and Ed, thanks for sharing your wisdom and showing me the ropes around the lab. Thanks to you, the lab became a great and fun place it is now. Jason, thanks for setting the example to the expression "to work hard". You have it all - lots of ideas, tremendous talent, and passion for work; I hope to see you a full professor before I finish my postdoc.

Abhay, you were my hero from the day I joined the group, your intelligence and creativity sometimes seemed almost intimidating; much of what I know about experiments I have learned from you. Thanks for both teaching me how to get and stay cold and for letting me into your project. I have no doubt about a great academic future in front of you, I have but one request - stay in the US for your professorship.

Alex, thanks for being a good friend. Your wisdom and intelligence helped me many times over the years. If now I can hard-solder and tell the difference between a hefeweizen and a blonde beer it is thanks to you.

On all of the projects I worked on, I collaborated with Ferdinand. I have yet to meet a better experimentalist or a better labmate - smart, passionate, hard-working. You taught me countless lessons about experiments and became my very good friend - I am very grateful for that. It was very hard not to get jealous on your excellence in whatever you were taking on be it nanofabrication or windsurfing. Just stay confident and only the sky will be your limit.

If it were not for Jack, I would not know much about programming. Thank you for that, and for being a good friend all these years. Remember, it just takes one hour to commute from Princeton to Manhattan, so I expect to see you often.

Jacob, it is in part due to you that I evolved from almost failing chemistry to starting my own nanoparticle synthesis. Thanks for that.

Thank you Josh for all the discussions ranging in topics from Kondo to Borat and for being a good friend.

Kiran, thanks for feeding me Indian food from time to time, I wish you the best of luck with the 3D magnet. Sufei, you are rapidly becoming a skilled experimentalist. Thanks for putting up with me for the last couple of months and good luck.

I was blessed to collaborate with a stellar undergraduate. Thiti, thank you and best of luck with your paper. I have learned a lot from group's postdocs - Sergey, Edgar, Ilya, Janice, you were an invaluable source of wisdom and advice. I would like to thank my special committee members - Paul McEeuen and Piet Brouwer. Your help and encouragement were a blessing.

McEuen and Buhrman groups - thanks for making Clark Hall basement a wonderful place it is. Thank you Scott, Vera, Marcus, Arend, Yuval, Sami, Shahal, Xinjian, Luke, Greg, Pat, Eric, Preeti, Nate, EiLeen, Phil.

A very special thank you for Eric Smith - his willingness to help is only surpassed by the depth of his physics knowledge. All I know about machining is due to Sned. Thank you for teaching me about Zen and the art of machining.

Life would have been sad without my friends in Ithaca. Saikat, Ben, Ribhu, Jahan, Faisal, Amar, Sharvari, Peter, Danya, Sahak, Ivan, Senya - thank you, guys. Camille, thank you were for putting up with me for all these years, you made my life much more enjoyable.

Finally, thanks to my parents for everything they have done for me. Mom and Dad, you are the best.

TABLE OF CONTENTS

1 Single electron transistors, single spins, and ferromagnetism 1
- 1.1 Introduction . . . 1
- 1.2 Single electron tunneling . . . 3
- 1.3 SET as a tool for probing quantum states . . . 6
- 1.4 Metallic single electron transistors . . . 9
- 1.5 Electrical transport in ferromagnets . . . 11
- 1.6 Single electron tunneling and ferromagnetism . . . 14
- 1.7 Realistic SET with ferromagnetic leads: how to make it and why is it hard? . . . 16
- 1.8 Outline . . . 18

Bibliography 20

2 Efficient gating in a metal-nanoparticle SET in horizontal geometry 22
- 2.1 Previous work and motivation . . . 22
- 2.2 Fabrication . . . 24
- 2.3 Measurements . . . 26

Bibliography 32

3 Using chemical tools to fabricate SETs 34
- 3.1 Introduction . . . 34
- 3.2 Nanoparticle synthesis techniques . . . 35
- 3.3 Gold nanoparticle synthesis . . . 37
- 3.4 Platinum and palladium nanoparticle synthesis . . . 38
- 3.5 Contacting nanoparticles: molecular self-assembly . . . 40
- 3.6 Alternative approaches to self-assembly . . . 47

Bibliography 51

4 Understanding the properties of nanometer-sized magnetic electrodes 53
- 4.1 Introduction . . . 53
- 4.2 Domain walls in narrow ferromagnets: contribution to the resistance 55
- 4.3 Prior work: the mystery of 1000% magnetoresistance . . . 58
- 4.4 Fabrication . . . 60
- 4.5 Measurements . . . 63

Bibliography 70

5 Anisotropic magnetoresistance due to quantum interference in ferromagnets **72**
5.1 Introduction 72
5.2 Brief overview: Mesoscopic conductance fluctuation due to quantum interference 73
5.3 Quantum interference in ferromagnets 76
5.4 AMR due to quantum interference: the experiment 77
5.5 Looking back: domain walls & quantum inteference 87

Bibliography **93**

6 Conclusions and possible experiments **95**
6.1 Progress towards ferromagnetic SETs 96
6.2 Electromigration after depositing the nanoparticles 101
6.3 Nanoparticle deposition inside the refrigerator 103
6.4 SETs with ferromagnetic electrodes: theoretical proposals 104
6.5 More proposals for future experiments 108

Bibliography **111**

LIST OF FIGURES

1.1 a) A diagram of a single-electron transistor (SET). (b) The current as a function of the voltage bias across the SET is suppressed at low bias voltage. (c) Coulomb blockade region in the $V - V_G$ plane; the number of electrons N and $N + 1$ on the SET's island is constant in time inside each region. The capacitance C_L, C_R, C_G can be extracted from the slopes $\frac{-C_G}{C_L+\frac{1}{2}}$ and $\frac{C_G}{C_R+\frac{1}{2}}$ of the sides of the region ($C = C_L + C_R + C_G$) and the spacing e/V_G between neighboring degeneracy points. 4

1.2 (a) Current as a function of bias across the SET. Steps in current are observed as individual states become available for tunneling. (b), (c), (d), (e) Different stages of electronic transport through an SET. (f) SET's conductance as a function of V and V_G. Particle-in-a-box states show up as lines in the $V - V_G$ plane. 7

1.3 Band structure of a typical metallic ferromagnet. The DOS for the d band is spin split by the exchange interaction. 11

1.4 (a) Tunneling between two ferromagnetic electrodes. The angle between magnetization M_L of the left and of the right M_R electrodes is θ. (b) A single-electron transistor with ferromagnetic leads. Non-trivial spin S can be accumulated on the island. 14

2.1 A cartoon of the device of Ralph *et al.* [9]. A nanometer-sized hole is used to make stable electrical contacts to a nanoparticle 23

2.2 (a) Top-view scanning electron microscope (SEM) image of the device geometry, with gold source and drain electrodes on top of an oxidized aluminum gate. (b) Expanded view of the region outlined with a white rectangle in (a). A 10-nm gap made by electromigration is visible, along with deposited gold nanoparticles. (c) Circuit schematic for the Au-nanoparticle SET. 25

2.3 . (a) Coulomb staircase $I - V$ curve for a gold nanoparticle SET (device #1) at 4.2 K, along with an orthodox model fit (offset for clarity). (b) $I - V$ curves for device #1 at 4.2 K, for equally spaced values of V_G. (c) Gray-scale plot of dI/dV as a function of V_G and V for device #1 at 4.2 K. Eleven degeneracy points separating twelve different charge states are visible within a 2 V range of V_G. (d) Gray-scale plot of dI/dV as a function of V_G and V for device #2 at 4.2 K, showing "Coulomb diamonds" as well as several abrupt changes in the background charge of the SET island as V_G is swept. 27

2.4 Gray-scale plots of dI/dV as a function of V_G and V, displaying the discrete electron-in-a-box level spectra within a gold nanoparticle (device #3), measured with an electron temperature less than 150 mK and zero magnetic field. Panels (a), (b), and (c) represent spectra for different numbers of electrons in the same nanoparticle. Panel (b) covers the gate voltage range from -95 mV to -110 mV and (c) the range from -180 mV to -195 mV. Insets: Energy-level diagrams illustrating the tunneling transitions that contribute to line for different numbers of electrons on the particle. 29

3.1 Gold nanoparticles (Ted Pella) of different sizes. The particles are highly spherical and monodisperse. 38
3.2 Palladium nanoparticles synthesized using the method of Choo *et al.* [16] 39
3.3 Platinum nanoparticles synthesized using the modified the method of Sarathy *et al.* [17]. 40
3.4 Using chemical self-assembly to place the nanoparticle onto the electrodes. A molecule with two functional endgroups may be used to attach the nanoparticle to the substrate. 41
3.5 The acidity of the gold nanoparticle solution can be adjusted to control the surface coverage of the nanoparticles. 43
3.6 Gold nanoparticle between two electodes resulting in a stable single electron transistor 44
3.7 Conductance (colorscale) as a function of bias and gate voltages for a chemically synthesized metallic nanoparticle SET. The island of the SET is a 15 nm gold nanoparticle (Ted Pella), APTS molecules bind the particle to the electrodes. 46
3.8 Gold nanoparticles are only deposited onto the electrode kept at the positive bias (on the left). 47
3.9 Gold nanoparticles are placed between the electrodes using electrostatic trapping. 50

4.1 Domain wall contributing to ferromagnet's resistance due to AMR. 56
4.2 (a) Scanning electron micrograph of a finished device. Gold electrodes are used to contact two permalloy thin-film magnets (inset) on top of an oxidized aluminum gate. The irregular shape of the Py electrodes results from imperfect liftoff during fabrication. (b) Micromagnetic modeling showing antiparallel magnetic alignment across the tunneling gap in an applied magnetic field of H= 66 mT. 61

4.3 The cross section of a constriction is reduced in stages (a,b,c) by repeatedly ramping the bias voltage until electromigration begins, and then quickly decreasing the bias, following a procedure similar to that in [18]. The SEM micrographs illustrate the gradual narrowing of the constriction, which appears bright in these images. Inset: Resistance as a function of magnetic field for a tunneling device exhibiting abrupt switching between parallel and antiparallel magnetic states. 62
4.4 (a) Magnetoresistance as a function of resistance in the range less than 400 Ω (device I). (b) Magnetoresistance as a function of resistance in the range 60 Ω - 15 kΩ (device II). Inset: Switching behavior of device II at different resistances (curves are offset vertically for clarity.) 64
4.5 The evolution of magnetoresistance in the tunneling regime (device III) as the resistance of the tunneling gap is changed by electromigration (curves are vertically offset for clarity). Inset: distribution of magnetoresistances for devices in the tunneling regime (> 20 kΩ). 66
4.6 Differential conductance as a function of bias voltage for device IV at small (a), intermediate (b) and large (c) resistances. (d) Magnetoresistance as a function of bias for a tunneling device (device V). 68

5.1 Cartoon diagram representing an electron's trajectory in diffusive metals when $\tau_e \ll \tau_\phi$. Circle represent elastic scattering from the impurities, squares represent inelastic scattering from phonons . . . 74
5.2 (a) Zero-bias differential resistance vs. angle of applied magnetic field at different field magnitudes at 4.2 K, illustrating bulk AMR for a constriction size of 30×100 nm^2 and resistance $R_0 = 70$ Ω (device A). (b) SEM micrograph of a typical device. 78
5.3 (a) Evolution of AMR in device B as its resistance R_0 is increased from 56 Ω to 1129 Ω. (b) AMR for a $R_0 = 6$ kΩ device (device C) exhibiting 15% AMR, and a $R_0 = 4$ MΩ tunneling device (device D), exhibiting 25% TAMR. All measurements were made at a field magnitude of 800 mT at 4.2 K. Inset: AMR magnitude as a function of R_0 for 12 devices studied into the tunneling regime. 79
5.4 Variations of $R = dV/dI$ at 4.2 K in a sample with average zero-bias $R_0 = 2.6$ kΩ (device E). (a) R vs. field angle at different bias voltages ($|B| = 800$ mT). (b) Dependence of R on V at different fixed angles of magnetic field ($|B| = 800$ mT). The curves in (a) and (b) are offset vertically. (c) R as a function of V and magnetic field strength, with field directed along the x axis. R does not have significant dependence on the magnitude of B. (d) R as a function of V and θ, for $|B| = 800$ mT. 81

5.5 Variations of $R = dV/dI$ at 4.2 K in a sample with average zero-bias $R_0 = 257$ kΩ (device F), in the tunneling regime. (a) R vs. field angle at different bias voltages ($|B| = 800$ mT). (b) Dependence of R on V at different fixed angles of magnetic field ($|B| = 800$ mT). The curves in (a) and (b) are offset vertically. (c) $R(V) - R_{\rm av}(V)$ as a function of V and magnetic field strength, with field directed along the x axis. $R_{\rm av}(V)$, the average of $R(V)$ over angle (shown in (b)), is subtracted to isolate angular-dependent variations. (d) $R(V) - R_{\rm av}(V)$ as a function of bias voltage and magnetic field angle, for $|B| = 800$ mT. 83
5.6 Domain wall contribution to the magnetoresistance for a 60 Ω permalloy device. (a) Change in resistance as a function of magnetic field angle. (b) Change in resistance as a function of magnetic field strength; the field is applied along the x axis (blue curve) and y axis (pink curve) 89
5.7 Domain wall contribution to magnetoresistance for a 7 kΩ permalloy device. (a) Change in resistance as a function of magnetic field angle. (b) Change in resistance as a function of magnetic field strength; the field is applied along the x axis (blue curve) and y axis (pink curve) 90
5.8 Domain wall contribution to mesoscopic interference for 19 kΩ permalloy device. (a) R(V) as a function of bias voltage and magnetic field angle, for $\|B\| = 800$ mT (b) R(V) as a function of magnetic field strength, with magnetic field directed along the x axis. Note the switching events near zero field. (c) R(V) as a function of bias voltage for $\|B\| = 6$ mT and $\|B\| = 8$ mT. Note the change in resistance. 92

6.1 Conductance (colorscale) as a function of gate and bias voltage for an SET with gold island and nickel electrodes. 97
6.2 Conductance (colorscale) as a function of magnetic field and bias voltage for a metallic SET with gold island and ferromagnetic (nickel) leads. Note the shift of particle-in-a-box states around +40 mT 97
6.3 Conductance (colorscale) as a function of the applied magnetic field from -8 T to +8 T and bias voltage for an SET with gold island and nickel electrodes. Note the asymmetry in the electron levels with respect to zero field. 98
6.4 The conductance of a ferromagnetic tunneling gap protected by aluminum and silicone oxide capping layers monitored after electromigration. The conductance slowly decreases as the chamber is vented with dry nitrogen and drops to zero as the chamber is opened to air, suggesting that ferromagnetic electrodes may be oxidized. . 100

6.5 (a) Electromigration of gold electrodes after a self-assembled monolayer of gold nanoparticles was deposited. Notice the absence of the nanoparticles next to the gap between the electrodes. (b) Same as (a), except that before electromigration the SAM of nanoparticles was treated with ethanol solution of hexenedithiol. Note the particles in the gap region. 102
6.6 (a) A filament is extracted from a conventional lightbulb. (b) The filament is placed next to the chip on a helium dipstick. 103
6.7 (a) After passing a current through the filament the metal deposited on the filament gets redeposited onto the surface of the chip (b) Some of the tunneling devices change their resistance and exhibit a Coulomb blockade after the evaporation. 105
6.8 The results of Martinek et al. [7]. (Reproduced with permission from Jan Martinek.) (a), (b) Current across a ferromagnetic SET as a function of bias voltage in the non-linear regime, for different polarizations p of the electrons at the Fermi level. (a) Magnetization in the left and right electrode directed in the opposite directions ($\theta = 180°$). (b) $\theta = 90°$. (c) Differential conductance of the SET in the linear response regime $eV < kT$ as a function of angle between the magnetization direction of the two electrodes θ, for different gate voltages ϵ. 106
6.9 The results of Martinek et al. [16]. (Reproduced with permission from Jan Martinek). Differential conductance across the SET in the linear response regime as a function of applied magnetic field, with magnetization of the leads aligned antiparallel. The width at half-maximum of the resonance is inversely proportional to the spin-relaxation time. 108

Chapter 1

Single electron transistors, single spins, and ferromagnetism

1.1 Introduction

Bohr is right after all.

W. Gerlach

In 1922, Otto Stern and Walther Gerlach directed a beam of silver atoms passing through a gradient of magnetic field onto a glass plate. The resulting thin film of metal was almost invisible, but when the smoke from Stern's cheap cigar turned silver into silver sulfide, two black lines clearly appeared on the plate [1]. The two lines signified two electron spin-states, marking the first observation of space quantization.

Much has changed over the last 80 years, and we do not have to rely on cigar smoke anymore: Thanks to MRI imaging, looking at collective spin properties has become a part of the everyday duties of a medical doctor in a big hospital. However, the interest in all things spin-related is on a big rise among physicists: the number of papers containing the word "spin" in the title, for example, increased more than tenfold between the years 1960 and 2005 [2]. This interest is at least in part due to the progress towards electrical creation and manipulation of spin-polarized electron currents. Suddenly, the electronic analog of optical experiments with polarized light became possible, with ferromagnets in place of optical polarizers and normal metals in place of optical fibers.

Such experiments are not solely motivated by sheer curiosity: employing the

electron's spin degree of freedom holds a great promise for the next generation of electronic devices. The emerging "spintronics" technology may offer higher degrees of integration, nonvolatility, and lower power consumption compared to traditional semiconducting technology [3, 4, 5]. Of course, our ability to manipulate the spin degree of freedom is far behind our ability to manipulate conventional electrical currents. We do not yet know, for example, how to obtain 100% polarized spin currents. Nevertheless, we can try looking into the future and consider the possibilities down the road assuming that spintronics follows the same avenue as electronics did. Nowadays semiconducting technology allows studying routinely tunneling of individual electrons [7], resolving single electronic quantum states [6], and even entangling the wavefunctions of two electrons [8]. We can imagine experiments with similar level of control for spins: Is it possible to detect a spin of a single electron? Can we create and measure a spin eigenstate? How robust can we make this eigenstate?

Broadly defined, this thesis tries to tackle some of these questions. Of course, the problems outlined above are very general (and hard, needless to say), so we focus on one particular example of a device which is capable of measuring spin eigenstates: the single electron transistor (or SET) with ferromagnetic electrodes. The work in this thesis has been started with the idea in mind to develop the basic building blocks for such an SET, and while we are at it, to explore the underlying physics. Over the years, some of the seemingly simple problems of understanding particular SET components became research topics of their own, and hence now this thesis includes topics ranging from mesoscopic interference in ferromagnets to chemical self-assembly of nanoparticle monolayers.

In this introductory chapter we briefly discuss the basics of single-electron tun-

neling and ferromagnetism refering the reader to in-depth reviews and previous theses whenever possible. We also review both experimental and theoretical progress towards spin manipulation in single electron transistors.

1.2 Single electron tunneling

The single-electron transistor (SET) is the most basic device probing the quantization of the electron's charge. A schematic of an SET is shown in Figure 1.1(a); its main components are the source electrode, the drain electrode, the gate electode, and the island which is separated from the rest of the electrodes by tunnel barriers. The device is a mesoscopic descendant of a conventional MOSFET and hence allows modulating the current flowing between the source and the drain electrodes by changing the gate voltage. Let us consider the SET in Figure 1.1(a), with capacitances of the island to the gate, right and left electrodes C_G, C_R, C_L respectively; the voltage applied to the gate, right and left electrode being V_G, V_R, V_L. The potential energy $E(N)$ of the island with N electrons is given by [20]

$$E(N) = \frac{e^2}{2C}(N - n_D)^2 - \frac{e^2}{2C}n_D^2, \tag{1.1}$$

$$n_D = (C_L V_L + C_R V_R + C_G V_G)/e \tag{1.2}$$

where $C = C_L + C_R + C_G$. The main energy scale of the Eq. (1.1) is set by the Coulomb energy $E_c = e^2/2C$; it can be understood as work required to add one electron to an isolated particle with the self-capacitance C. While negligible for a conventional transistor, for a very small device the Coulomb energy may become a dominant energy scale. For example, for a 15 nm metallic sphere we can estimate $E_c \sim 100$ meV.

For an SET at low temperature $kT \ll E_c$, energy conservation requires that

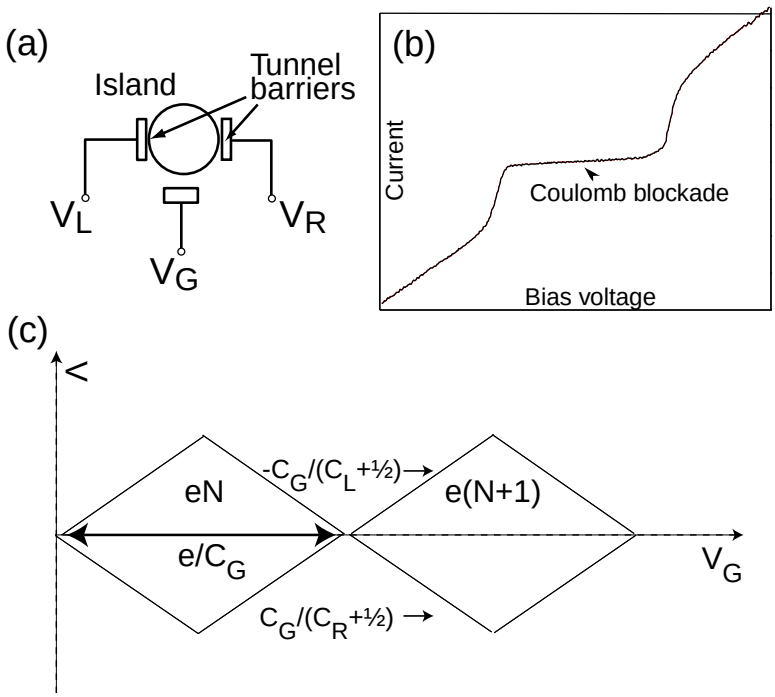


Figure 1.1: a) A diagram of a single-electron transistor (SET). (b) The current as a function of the voltage bias across the SET is suppressed at low bias voltage. (c) Coulomb blockade region in the $V - V_G$ plane; the number of electrons N and $N+1$ on the SET's island is constant in time inside each region. The capacitance C_L, C_R, C_G can be extracted from the slopes $\frac{-C_G}{C_L+\frac{1}{2}}$ and $\frac{C_G}{C_R+\frac{1}{2}}$ of the sides of the region ($C = C_L + C_R + C_G$) and the spacing e/V_G between neighboring degeneracy points.

an electron from the left (right) lead may tunnel onto the island with the initial charge eN when

$$E(N+1) - E(N) \leq eV_{L(R)}. \tag{1.3}$$

Similarly, an electron may leave the island with charge $e(N+1)$ to tunnel into the left(right) lead when

$$E(N+1) - E(N) \geq eV_{L(R)}. \tag{1.4}$$

The conditions (1.4) and (1.3) indicate that electrons tunnel from and onto the island as to minimize its potential energy $E(N)$; the equation (1.1) indicates that the equilibrium electron number N is simply given by the integer closest to n_D. We also note that n_D explicitly depends on the gate voltage V_g, providing a convenient "knob" to adjust the equilibrium number of electrons on the island.

When N is at minimum both conditions Eq. (1.3) and Eq. (1.4) are violated for small bias voltage and tunneling is suppressed (Coulomb blockade). The case of half-integer $n_D = N + \frac{1}{2}$ is exceptional: tunneling is possible at zero bias because $E(N+1) - E(N) = 0$ (Eq. (1.1)), and the SET is said to be at its degeneracy point. As a result the current across the SET at small bias $V < kT$ exhibits "Coulomb oscillations" as a function of gate voltage with period ΔV_G determined by the condition

$$\Delta V_G = e/C_G. \tag{1.5}$$

When the bias voltage $|V_{L(R)}|$ exceeds $E(N+1)-E(N)$ the Coulomb blockade is lifted, as the battery can provide enough energy to change the number of electrons on the island by one, but not more. Thus, current can start to flow by shuttling one electron first onto the island across the left tunnel barrier and then off the island across the right tunnel barrier (Fig. 1.1(b)).

In our experiments we typically measure the conductance of the SET as a function of both gate V_G and bias $V = V_L = -V_R$ voltage (symmetric biasing) in order to extract the effective capacitances C_L,C_R, and C_G of Figure 1.1(a). In $V - V_G$ plane, the region of Coulomb blockade is diamond-shaped, with the constraints Eq. (1.3) and Eq. (1.4) determining the slopes of the diamond's sides; Figure 1.1(c) illustrates the process of determining the capacitances from the shape of the Coulomb diamonds.

1.3 SET as a tool for probing quantum states

Quantum-mechanical confinement leads to another qualitative change as an SET's size gets smaller. This occurs when the particle-in-a-box level spacing of the island becomes comparable to the temperature. In that case the density of states of the island can no longer be considered continuous; individual particle-in-a-box states spaced an average Δ apart contribute to transport. Experimentally, fine features due to tunneling through individual particle-in-a-box states appear on top of the non-linear conductance due to the Coulomb blockade (Fig. 1.2(a)).

Let us consider how this happens: Let's assume that at zero bias voltage the energy of the N electron ground states e_N is equal to the energy of the N+1 electron ground state $e_N + 1$. In this case electrons are shuttled through the SET by first tunneling from the left lead into the island thus bringing it to the N+1 electron ground state (Fig. 1.2(b)) and then from the island into the left lead, leaving the island in the N electron ground state (Fig. 1.2(c)).

Let us now imagine that the bias voltage is increased and an electron from the right lead can tunnel into either of the two single-electron levels (Fig. 1.2(d)); the tunneling rate in this situation is given by the sum of the tunneling rates for

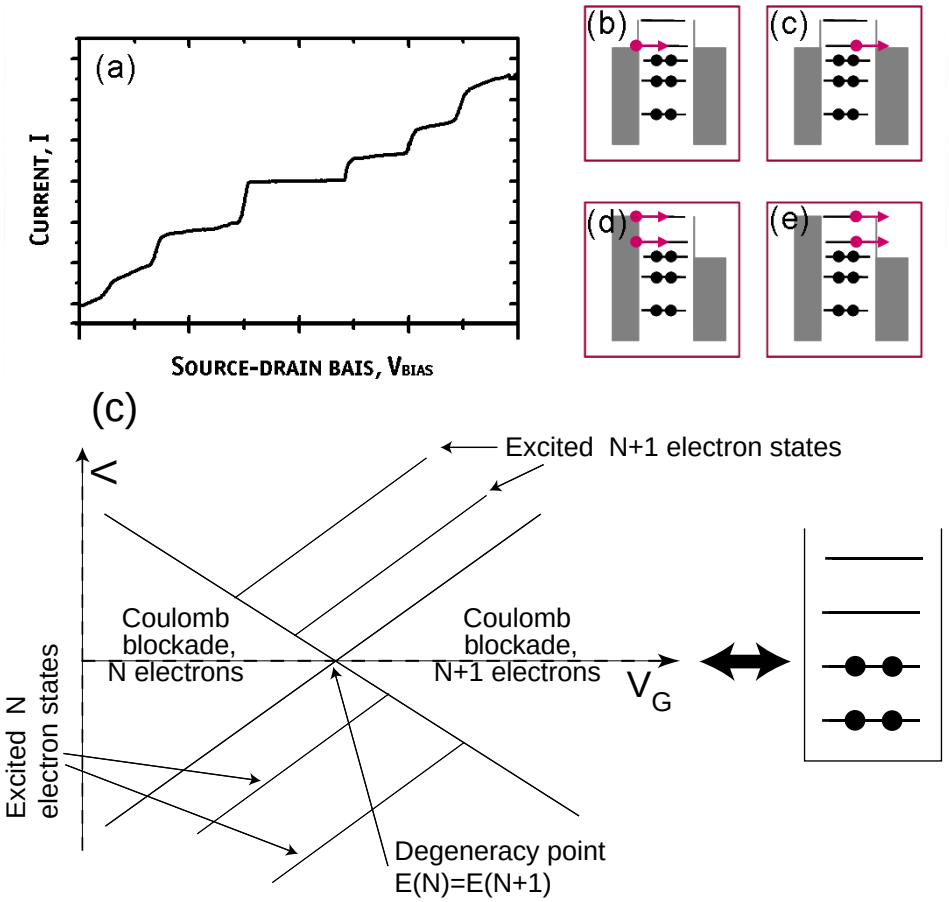


Figure 1.2: (a) Current as a function of bias across the SET. Steps in current are observed as individual states become available for tunneling. (b), (c), (d), (e) Different stages of electronic transport through an SET. (f) SET's conductance as a function of V and V_G. Particle-in-a-box states show up as lines in the $V - V_G$ plane.

both states. Then the electron from either state can tunnel out into the right lead (Fig. 1.2(e)), once again at the increased rate. Hence, as a new state becomes available for tunneling, the tunneling rates (and the current) increase. We can thus see than the current across the SET increases in steps (Fig. 1.2(a)), with each step corresponding to the Fermi level of one of the electrodes aligned with a single-electron level inside the particle.

Quantitatively, when individual single-electron levels are taken into account equation (1.1) gives the energy of the island with N electrons in the *ground* state. We can express the energy of the excited state $|\alpha\rangle$ by adding the term $\epsilon_\alpha(N) > 0$ to Eq. (1.1). In that case, state $|\alpha\rangle$ contributes to tunneling of electrons to (from) the particle when the modified Eqs. (1.3) and Eq. (1.4) hold true

$$E(N+1) - E(N) + \epsilon_\alpha(N+1) \leq eV_{L(R)}, \tag{1.6}$$

$$E(N+1) - E(N) - \epsilon_\alpha(N) \geq eV_{L(R)}. \tag{1.7}$$

These equations define a set of lines in the $V - V_G$ plane (Fig. 1.2(f)); SET conductance measurement as a function of bias and gate voltage allows visual extraction of both occupied and unoccupied single-electron levels. In order to determine the energies of the particle-in-a-box states the capacitance ratios determined as in Fig. 1.1(c) should be taken into account.

Three conditions should be fulfilled for to resolve single-electon energy levels [20]:

- The temperature kT must be smaller than the level spacing Δ
- The tunneling rates Γ of the states should be small enough so that the tunnel-induced level width $\hbar\Gamma$ does not cause the neighboring levels to overlap.

- For the same reason, the inelastic relaxation rate for the excited states Γ_{inel} should be small enough so that the corresponding linewidth $\hbar\Gamma_{inel}$ is smaller the the level spacing Δ.

If all of the above conditions are met we can extract a wealth of information about the quantum-particle-in-a-box states of the SET by means of conductance measurements. In addition to the positions of both occupied and unoccupied electronic states we can estimate the tunnel couplings of individual state to the electrodes and in some cases the lifetimes of the excited states [11].

1.4 Metallic single electron transistors

As we have seen, SETs can be used as a tool for studying quantum states in confining potentials. Very basic quantum mechanical problems can therefore be studied, ranging from the influence of the confining potential's shape on the distribution of the quantum states to the interplay of superconductivity and quantum confinement. Several experimental approaches to fabricate SETs are available depending on the problem one wants to study. We briefly mention three very different fabrication strategies: 2-DEG SETs (or quantum dots), carbon nanotube SETs, and metal nanoparticle SETs.

Single electron transistors are routinely fabricated by employing electrostatic gates defined on top of a two-dimensional electron gas (2-DEG) in GaAs/AlGaAs heterostructures [27]. A negative voltage applied to the gates results in pinching off a "puddle" from the electron sea, forming a single electron transistor. The geometry of the SET may be adjusted by changing the gate voltages to fine-tune the Coulomb energy, level spacing and tunnel couplings. However, the physics that can be accessed using such SETs is limited by the materials compatible with

semiconducting technology. In particular, it is very hard or impossible to fabricate 2-DEGs manifesting many-body effects such as superconductivity or magnetism.

Due to its one-dimensional nature, a carbon nanotube is an excellent choice for the island of an SET. Nanotubes are typically contacted using top evaporated metallic electrodes on top of a silicon or metal gate; both single-electron charging and transport through individual electronic states have been demonstrated in carbon-nanotube SETs [9]. Due to its low atomic weight (and small spin-orbit interaction) carbon is considered a promising material for spintronics applications, and controllable spin-injection into nanotubes has recently attracted a lot of interest [14].

In this thesis we focus on the third approach, using a mesoscopic metallic grain connected to metallic electrodes as the SET. The main advantage of the approach is the extent of the physics which can be accessed: the metal of either island or electrodes can be chosen ferromagnetic, antiferromagnetic or superconducting allowing the study of different aspects of correlated electron physics. Of course, there is a price to pay for this versatility: The electron density of a typical metal is very large compared to semiconductors and in order to resolve individual particle-in-a-box states, the island of a metallic SET needs to be nanometer-sized. Let us look at some numbers: The energy level spacing Δ of a metallic particle can be estimated in free-electron model as [20]

$$\Delta = \frac{2\pi^2\hbar^2}{mk_F V}, \tag{1.8}$$

where k_F is the Fermi wavevector, V is particle's volume, and m is electron's effective mass. In order to observe quantum confinement effects and to study the transport through particle-in-a-box states in a metallic nanoparticle, the energy level spacing Δ needs to be larger than the temperature kT. For T $\sim$100 mK

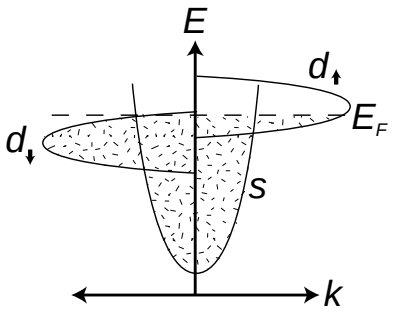


Figure 1.3: Band structure of a typical metallic ferromagnet. The DOS for the d band is spin split by the exchange interaction.

(typical electron temperature in a dilution refrigerator base temperature) and a typical metal with $k_F \sim 10$ nm^{-1} this sets an upper limit of 20 nm on the size of the island of the SET.

Clearly, such an SET cannot be fabricated using conventional electron beam lithography (EBL): the island of the SET should be aligned with respect to the electrodes with near-nanometer accuracy, more than by a factor of 20 smaller than what EBL allows; this alone makes fabricating such an SET a complicated task.

1.5 Electrical transport in ferromagnets

Conductance measurements similar to the ones discussed above may be used to probe precession, relaxation, and decoherence of single spins in SETs with ferromagnetic leads. Electrical transport in a ferromagnet however is sensitively coupled to its magnetization direction (magnetoresistive effects), complicating interpretation of conductance measurements. Thus, before discussing ferromagnetic SETs, in this section we briefly review the basics of magnetotransport in ferromagnets.

The band structure of a ferromagnet is markedly different from that of a normal metal. A typical metallic ferromagnet (Ni, Co, Fe) has partially filled $4s$ and $3d$

electron bands. The density of states of the d band is spin-split by the exchange interaction; the majority spin states (along magnetization direction) are shifted with respect to the minority spin states (antiparallel to the magnetization), as shown in Figure 1.3. As a result, the DOS at the Fermi level differs between majority and minority electrons, as quantified by the polarization ratio

$$p = \frac{\nu^{\uparrow} - \nu\downarrow}{\nu^{\uparrow} + \nu^{\downarrow}}, \tag{1.9}$$

where $\nu^{\downarrow}$ and $\nu^{\uparrow}$ is the density of states for minority and majority electrons at the Fermi level. Nickel, for example, has a polarization ratio of $\sim 20\%$.

While the distinction between the delocalized s states and more localized d states is important (for instance, the anisotropy in magnetoresistance is caused by $s-d$ scattering), phenomenological models of electrical transport in ferromagnets neglect the difference between s and d electrons. The transport is then described in terms of the so-called "two current model", treating the currents of spin-up and spin-down electrons independently.

There are several magnetoresistive (MR) effects that couple the magnetization of ferromagnets to their transport properties. We briefly mention two of them, anisotropic magnetoresistance (AMR) and tunneling magnetoresistance (TMR).

Anisotropic magnetoresistance is the dependence of a ferromagnet's resistance ΔR on the angle ϕ between the magnetization direction and the direction of current:

$$\Delta R \sim cos^2(\phi) - 1/2 \tag{1.10}$$

AMR is caused by the anisotropy in electron scattering due to spin orbit interaction and is typically a small effect in most materials ($\Delta R/R < 1\%$). Much of the research into AMR effect is motivated by the interest from magnetic recording industry; until recently the AMR effect was used in every hard-drive read-head.

Tunneling magnetoresistance is observed for a system of two ferromagnetic electrodes separated by a tunneling gap (a spin valve); in such a system the tunneling current acquires a dependence on the angle between the magnetization vectors of the two electrodes (Fig. 1.4(a)). TMR can be easily (albeit not very accurately) explained using Fermi golden rule considerations. Following Julliere [23], we can estimate the tunneling current I_P for the parallel alignment of the leads using the two current model and assuming spin conservation during tunneling

$$I_P \propto \nu_{\uparrow L}\nu_{\uparrow R} + \nu_{\downarrow L}\nu_{\downarrow R}, \tag{1.11}$$

where $\nu_{\sigma r}$ is the spin-resolved DOS at the Fermi level in either left ($r = L$) or right ($r = R$) lead. Similarly, for an antiparallel configuration of the leads we obtain

$$I_{AP} \propto \nu_{\uparrow L}\nu_{\downarrow R} + \nu_{\downarrow L}\nu_{\uparrow R}, \tag{1.12}$$

For the case of the same material right and left electrodes ($\nu_{L\sigma} = \nu_{R\sigma}$) we get $I_{AP} < I_P$ or, in other words, the resistance of a spin-valve in minimal when the magnetization of the electrodes is aligned. Quantitatively, the TMR can be described by the magnetoresistance ratio

$$TMR = \frac{I_P - I_{AP}}{I_{AP}} = \frac{2p_L p_R}{1 - p_L p_R} \tag{1.13}$$

Typical values for the magnetoresistance of ferromagnet-metallic oxide-ferromagnet structures are in the range of tens of percent, however recently the TMR ratios in excess of 100% were reported at room temperature (e.g. [25] and references therein).

The equation (1.13) may be generalized for an arbitrary angle θ between $\mathbf{M_L}$ and $\mathbf{M_R}$ [24]:

$$\frac{I(\theta) - I_{AP}}{I_{AP}} = \frac{2p_L p_R}{1 - p_L p_R} cos^2(\frac{\theta}{2}) \tag{1.14}$$

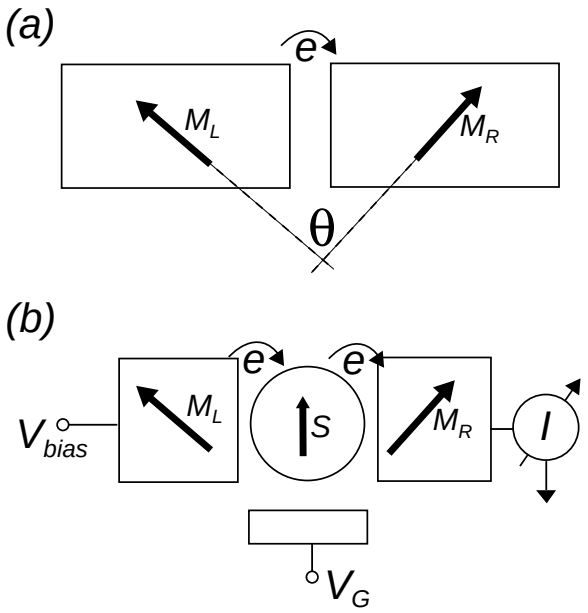


Figure 1.4: (a) Tunneling between two ferromagnetic electrodes. The angle between magnetization M_L of the left and of the right M_R electrodes is θ. (b) A single-electron transistor with ferromagnetic leads. Non-trivial spin S can be accumulated on the island.

Although this expression has a similar functional form to that of AMR (1.10) the size of the TMR effect is much larger; the mechanism of TMR has to do with electron tunneling compared to the spin-dependent scattering in case of AMR.

1.6 Single electron tunneling and ferromagnetism

Embedding a metallic grain between two ferromagnetic electrodes significantly changes the simple picture of spin-polarized tunneling. Several factors contribute to the complexity of the resulting single-electron transistor with spin polarized leads (Fig. 1.4(b)) compared to its normal-metal counterpart:

- Depending on the polarization of the electrodes, the left and right tunnel

barriers may preferentially transmit the electrons of different spin. In that case, at finite bias voltage a non-trivial spin can be accumulated on the dot. The accumulated spin depends on the angle θ between magnetization direction of the two leads.

- The accumulated spin precesses in an applied magnetic field, making a simple description of the SET in terms of rate equations for two spin components impossible.

- The tunneling of the electrons between the island and the leads may be described in terms of an effective magnetic field; the electron precesses in this field even in the absence of the external field.

- Accumulated spin modifies the DC conductance across the SET.

SETs with spin-polarized leads were demonstrated in several recent experiments:

- In the approach of Ono *et al.* [13] a lithographically-fabricated aluminum island was contacted using ferromagnetic electrodes, allowing the observation of single-electron charging.

- Sahoo *et al.* [14] succeded in contacting an individual nanotube using $PdNi$ alloy electrodes and studied gate-voltage dependent magnetoresistance in such a spin valve.

- Pasupathy *et al.* [21] fabricated a single molecule SET in the regime of strong coupling to the leads to study the coexistance of Kondo effect and ferromagnetism.

- Davidovic *et al.* [22] studied conductance through a network of metallic

clusters sandwiched between two ferromagnetic electrodes and observed signatures of the Hanle effect.

Despite the number of publications, the field of single-spin manipulation is in its infancy; there is a lot of room for new, better controlled experiments. Leaving more detailed discussion of the underlying physics for later, we mention the theoretical prediction of Braig *et al.* [10] concerning the case of a quantum dot with several quantum levels and highly spin-polarized electrodes. Braig *et al.* showed that the step heights of Figure 1.2(a) change between parallel and antiparallel orientation of the electrodes' magnetization. This distinct experimental signature indicates both the spin-accumulation on the SET's island and the interplay of spin-accumulation and electronic transport.

1.7 Realistic SET with ferromagnetic leads: how to make it and why is it hard?

As we have seen, an SET with ferromagnetic leads provides an exciting playground for the manipulation of single spins. Let us now consider closely how different components of the idealized device (Figure 1.4(b)) may be achieved experimentally and what kind of problems we are likely to encounter.

Electrodes with high degree of spin polarization First, we need ferromagnetic leads with high degree of polarization p of the electrons at the Fermi level. Polarization ratios for metallic ferromagnets are not very high: e.g. $\sim 30\%$ for iron, $\sim 20\%$ for cobalt [28]. Magnetic semiconductors can be engineered to reach higher p, but making a reliable contact to such semiconductors, however, is a formidable and currently unsolved task.

Ferromagnetic materials are notoriously tricky to engineer at the nanoscale. First, metallic ferromagnets (Ni, Co, Fe) oxidize in ambient atmosphere, resulting in deteriorated magnetic properties. Second, ferromagnets tend to change their shape as magnetic field is applied and special care needs to be taken to avoid artifacts related to this mechanical motion. Finally, while little experimental work has been done on near-atomically-narrow ferromagnets, the theory hints that their magnetic and transport properties may be dominated by quantum effects.

Nanoscopic SET island As discussed earlier, the requirement of resolving quantum states in a nanoparticle puts an upper limit on the size of SET's island to about twenty nanometers, ruling out e-beam lithography as the primary fabrication tool. For the same reason, shadow-evaporation-like techniques [18] are also out of the question. Most of the alternative pathways to the problem rely on self-assembly as part of the fabrication and all share a very low yield of working devices [17].

Material of the SET island Spin-orbit (SO) interaction can significantly perturb the electronic eigenstates of the nanoparticle by mixing spin-up and spin-down states [12]. We can avoid this mixing by choosing the material of the SET island to have a low atomic number Z, as the strength of SO interaction scales as Z^4. Aluminum, with a Z of 13 has been a metal of choice for spintronics experiments; all-aluminum SETs have been fabricated in the past [19]. However, aluminum readily oxidizes in air and special care should be taken to avoid unwanted oxidation.

Well-coupled gate electrode For the tunneling current to flow through just one

quantum state, the SET needs to operate near its degeneracy point, where the energies of two states differing by one electron are equal. The relative energies of the two states can be adjusted using the gate electrode. An efficient gate electrode can also serve as a knob for tuning the number of electrons on the island; this control is important for some of the experiments described in this thesis. For efficient gating, the gate electrode needs to be as close to the island as possible. Ideally, the gate is separated from the island only by a thin ($\sim$ 3 nm) layer of gate oxide. The challenge here is to fabricate highly uniform pinhole-free oxide compatible with the rest of the fabrication.

Controlled tunnel barriers The choice of the optimal tunnel coupling between the island of the SET and the electrodes is a result of a trade-off: In order to observe the unperturbed particle-in-a-box states we would like the coupling to be as small as possible. Experimentally, however, the largest resistance we can measure reliably is of the order of tens of gigaohms, which sets the lower limit on the tunnel coupling. Thus, it is advantageous to control the tunnel barriers separating the island of the SET from the electrodes. Metallic oxides have been used in the past to form controlled tunnel barriers in SETs. In our setup, however, we would like to avoid oxidization of ferromagnetic electrodes, which makes the use of oxide tunnel barriers problematic.

1.8 Outline

This thesis is largely focused on realizing the components needed for ferromagnetic SETs and understanding the underlying physics; each chapter is roughly focused

on a different component of the device.

In the second chapter, we discuss our strategy for realizing an efficient gate electrode. We fabricate our model normal-metal SET in a horizontal geometry in order to test the gate action. We are able to tune the charge of the island by more than 30 electrons and observe the evolution of quantum states as electrons are added to the island one-by-one.

In the third chapter we describe progress towards controlling the island and the tunnel barriers of the SET using chemical self-assembly. We fabricate SETs using chemically synthesized nanoparticles of well-controlled size and composition and thiolated molecules serving as tunnel barriers.

The design, fabrication and understanding the properties of nanoscale magnetic electrodes is the focus of the fourth chapter. We use controlled electromigration to fabricate ferromagnetic breakjunctions with large predictable TMR. We then use the same setup to study the scattering of electrons by atomically sharp magnetic domain walls.

In the fifth chapter we discuss physics of magnetotransport in nanoscale ferromagnetic junctions. Angle resolved measurements of magnetotransport reveal that quantum interference plays an important role in electronic transport in atomic-sized ferromagnetic contacts. We observe mesoscopic conductance fluctuations in ferromagnetic point contacts and examine their contribution to the increased AMR of the devices.

Finally, in the last (sixth) chapter, we review the work done in this thesis and discuss the possibilities for new experiments.

BIBLIOGRAPHY

[1] O. Stern, *in Les Prix Nobel en 1946*, Imprimerie Royale Norstedt and Soner, Stockholm (1948), p. 123.

[2] According to the Web of Science^{TM}. The increase is not caused by a mere difference in the number of papers: the number of papers containing generic terms in the title (such as "resonance") did not change significantly between the same years.

[3] S. A. Wolf, D. D. Awschalom, R. A. Buhrman, J. M. Daughton, S. von Molnar, M. L. Roukes, A. Y. Chtchelkanova, and D. M. Treger, *Science* **294**, 1488 (2001).

[4] G. Prinz, *Science* **282**, 1660 (1998).

[5] I. Zutic, J. Fabian, and S. Das Sarma, *Rev. Mod. Phys.* **76**, 323 (2004).

[6] D. R. Stewart, D. Sprinzak, C. M. Marcus, C. I. Duruoz, and J. S. Harris, Jr., *Science* **278**, 1784 (1997).

[7] L. M. K. Vandersypen, J. M. Elzerman, R. N. Schouten, L. H. Willems van Beveren, R. Hanson, and L. P. Kouwenhoven, *Appl. Phys. Lett.* **85**, 4394 (2004).

[8] A. C. Johnson, J. R. Petta, J. M. Taylor, A. Yacoby, M. D. Lukin, C. M. Marcus, M. P. Hanson, and A. C. Gossard, *Nature* **435**, 925 (2005).

[9] M. Bockrath, D. H. Cobden, P. L. McEuen, N. G. Chopra, A. Zettl, A. Thess, and R. E. Smalley, *Science* **275**, 1922 (1997).

[10] S. Braig and P. W. Brouwer, *Phys. Rev. B* **71**, 195324 (2005).

[11] M. Deshmukh, *Ph. D. Thesis* (2002).

[12] J. Petta, *Ph. D. Thesis* (2003).

[13] K. Ono, H. Shimada, and Y. Ootuka, *J. Phys. Soc. Jpn.* **66**, 1261 (1997).

[14] S. Sahoo, T. Kontos, J. Furer, C. Hoffmann, M. Graber, A. Cottet, and C. Schonenberger, *Nature Physics* **1**, 99 (2005).

[15] X. Waintal and P. W. Brouwer, *Phys. Rev. Lett.* **91**, 247201 (2003).

[16] J. Martinek, Jozef Barnas, S. Maekawa, H. Schoeller, and G. Schon, *Phys. Rev. B* **66**, 014402 (2002).

[17] D. L. Klein, R. Roth, A. K.L.Lim, A. Paul Alivisatos, and Paul L. McEuen, *Nature* **389** , 699 (1997).

[18] T. A. Fulton and G. J. Dolan, *Phys. Rev. Lett.* **59**, 109 (1987).

[19] D. C. Ralph, C. T. Black, and M. Tinkham, *Phys. Rev. Lett.* **78**, 4087 (1997).

[20] J. von Delft and D. C. Ralph *Phys. Rep* **345**, 61 (2001).

[21] A. N. Pasupathy, R. C. Bialczak, J. Martinek, J. E. Grose, L. A. K. Donev, P. L. McEuen, and D. C. Ralph, *Science* **306**, 86 (2004).

[22] L. Y. Zhang, C. Y. Wang, Y. G. Wei, X. Y. Liu, and D. Davidovic, *Phys. Rev. B* **72**, 155445 (2005).

[23] M. Julliere, *Phys. Lett A* **54**, 225 (1975).

[24] J. C. Slonczewski, *Phys. Rev. B* **39**, 6995 (1989).

[25] S. S. P. Parkin, C. Kaiser, A. Panchula, P. M. Rice, B. Huges, M. Samant, and S-H Yang, *Nature Mat.* **3**, 862 (2004).

[26] S. I. Kiselev, J. C. Sankey, I. N. Krivorotov, N. C. Emley, R. J. Schoelkopf, R. A. Buhrman, and D. C. Ralph, *Nature* **425**, 380 (2003).

[27] S. Datta, *Electronic transport in mesoscopic systems*, Cambridge University press (1995).

[28] R. O'Handley, *Modern magnetic materials*, Wiley (2000).

Chapter 2

Efficient gating in a metal-nanoparticle SET in horizontal geometry

2.1 Previous work and motivation

Still round the corner there may wait,

A new road or a secret gate.

J. R. R. Tolkien

Our first goal is to establish electrical contacts to a metallic grain small enough to exhibit electron level quantization due to confinement at dilution refrigerator temperatures. As outlined in the introductory chapter, this means that the contacts should be aligned with respect to the grain with a near-nanometer accuracy, ruling out conventional lithographic techniques as a primary fabrication method. In addition, in order to study the transport through individual electron states, an efficient gate electrode is required. Several groups have tried to push the resolution limits of e-beam lithography (EBL) to study such ultra-small SETs. Pashkin *et al.* [10] used shadow evaporation in combination with EBL to fabricate an SET with an island smaller than 10 nm. The gate capacitance, however, was so small ($< 10^{-20}$ F) in the approach of Pashkin *et al.* that the charge of the island could not be adjusted by more than one electron.

Electron level quantization in a nanometer-sized metallic grain has been reliably demonstrated by Dan Ralph and co-workers [8]. Stable electrical contact to a grain was achieved by first "drilling " a hole in a suspended silicon nitride membrane using reactive ion etching and a top metallic electrode was deposited by

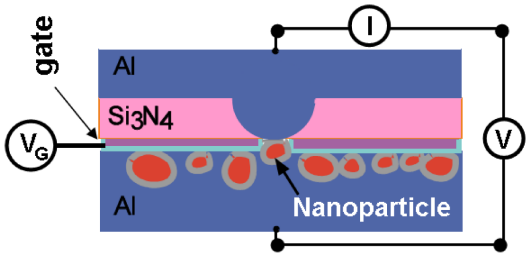


Figure 2.1: A cartoon of the device of Ralph *et al.* [9]. A nanometer-sized hole is used to make stable electrical contacts to a nanoparticle

thermal evaporation of aluminum (Fig. 2.1). A submonolayer of metal was then evaporated from the other side, and nanometer-sized particles self-assembled under the influence of surface tension. The tunnel barriers were formed by letting oxygen into the chamber and letting the oxidation form tunnel barriers on both side of the device. The device fabrication was finalized by depositing a bottom aluminum electrode (Fig. 2.1). This fabrication method was proven to be versatile; the interplay of superconductivity and quantum confinement, nanoscale ferromagnetism and the spin-orbit interaction were studied using this geometry. However, in order to produce the ultimate SET design for studying particle-in-a-box states in metals we would like to improve on several shortcomings of the design of Fig. 2.1:

- Efficient gate electrode adjusting the charge of the island is very hard to implement; the yield of devices with good gate action is prohibitively low.
- Direct imaging of the device is not possible.
- The particle size, shape and composition are poorly controlled.

In this chapter we describe our progress towards resolving the first two of the shortcomings. We fabricate metal-nanoparticle SETs in a horizontal geometry

with gate capacitances of order 10^{-18} F, sufficient to tune the number of electrons in a nanoparticle by more than ten. We use these devices to study the evolution of the electron-in-a-box level spectrum in gold nanoparticles as the electron number is changed one by one.

In the next chapter we focus on the last listed shortcoming, and use chemical self-assembly to both fabricate the island of the SET and control the tunnel barriers separating the island from the electrodes.

2.2 Fabrication

Our fabrication technique builds upon work in which electrical contact was made to single nanoparticles without a gate electrode [10, 11, 12, 13] and to networks of particles in the presence of a gate [14]. We start by using photolithography to define a 16-nm-thick Al gate electrode with 2 nm of Ti as a sticking layer, on top of an oxidized Si substrate. The gate electrode is deposited with the substrate at liquid nitrogen temperature. The Al is warmed overnight to room temperature while in 50 mtorr of oxygen and then exposed to air [15]. Next we use electron-beam lithography and liftoff to fabricate Au wires with a thickness of 16 nm and a minimum width of 100 nm on top of the gate (Fig. 2.2a). After cleaning the Au wires in oxygen plasma, we submerge the chip in liquid helium and break the wires using electromigration [16]; a source-drain bias is slowly ramped up until the wire breaks and the conductance drops suddenly [17]. In most cases this happens at a bias of ~ 1 V, and results in a gap about 5-10 nm wide after the sample is warmed to room temperature (Fig. 2.2b). A similar process of electromigration has been used recently to make single-molecule transistors [18, 19]. Then we create nanoparticles, formed by self-assembly, by evaporating Au on top of the broken

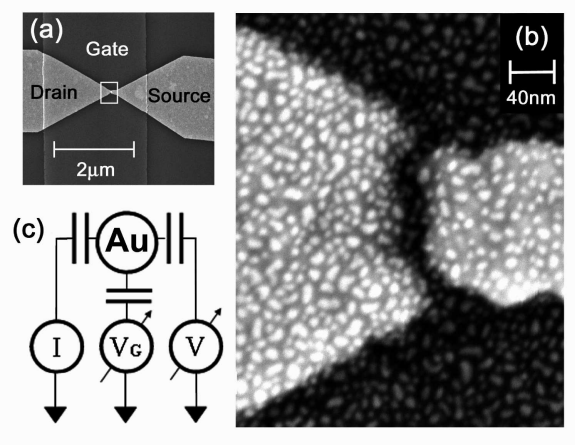


Figure 2.2: (a) Top-view scanning electron microscope (SEM) image of the device geometry, with gold source and drain electrodes on top of an oxidized aluminum gate. (b) Expanded view of the region outlined with a white rectangle in (a). A 10-nm gap made by electromigration is visible, along with deposited gold nanoparticles. (c) Circuit schematic for the Au-nanoparticle SET.

lines and into the gap with the substrate at room temperature. For most samples we evaporate 20 $\mathring{A}$ of gold at 0.6 $\mathring{A}$/s, which produces particle diameters of 5-15 nm as measured via SEM (Fig. 2.2b). When measured immediately after the evaporation, approximately 25% of the junctions show a drop of resistance into the MΩ range, indicating that a nanoparticle may be bridging the gap. This procedure has the virtue of producing nanoparticles separated from the gate electrode by only 2-3 nm of aluminum oxide, giving excellent coupling between the particle and the gate. Finally the devices are protected by evaporating 100 nm of aluminum oxide prior to air exposure.

2.3 Measurements

We cool the finished devices to 4.2 K and measure their current-voltage ($I-V$) curves as a function of gate voltage (V_G) (see Fig. 2.2c for circuit conventions). More than 50% of the devices that show a decrease in resistance during the nanoparticle deposition step exhibit Coulomb-blockade characteristics (Fig. 2.3a and 2.3b). Fits to the orthodox theory of Coulomb blockade [20] yield good agreement (Fig. 2.3a). The variation of dI/dV as a function of V_G and V is shown in Fig. 2.3c, for a range of V_G large enough to span several "Coulomb diamonds". The presence of only one positive and one negative slope for the tunneling thresholds vs. V_G indicates that transport is indeed occurring through a single nanoparticle [21]. The gate capacitance C_G is determined from the spacing in V_G between the degeneracy points where dI/dV is nonzero at $V = 0$. For device #1 (Fig. 2.3a-c), the spacing between neighboring degeneracy points is 180 mV, so C_G = e/(180 mV) = 0.89 aF ($\pm$5 %). This is an order of magnitude greater than gate capacitances achieved previously in metal nanoparticle transistors [9]. The ratios C_D/C_G and C_S/C_G for the drain and source capacitances are then determined from the slopes of the tunneling thresholds vs. V_G [22], yielding for device #1 $C_D = 2.4$ aF and $C_S = 1.3$ aF ($\pm$10 %). Fig. 2.3c demonstrates that 12 different charge states within this nanoparticle can be accessed by varying V_G within the range $\pm$1 V. We should note that the scan in Fig. 2.3c is somewhat atypical in that there are very few discontinuities in the gate-voltage dependence, corresponding to sudden rearrangements in the background charge near the particle. The diamond plot in Fig. 2.3d, from device #2, is more typical.

The yield given by our fabrication process is that 15-20% of all devices exhibit gate-dependent Coulomb blockade. The gate capacitances are typically 0.3-2.0 aF

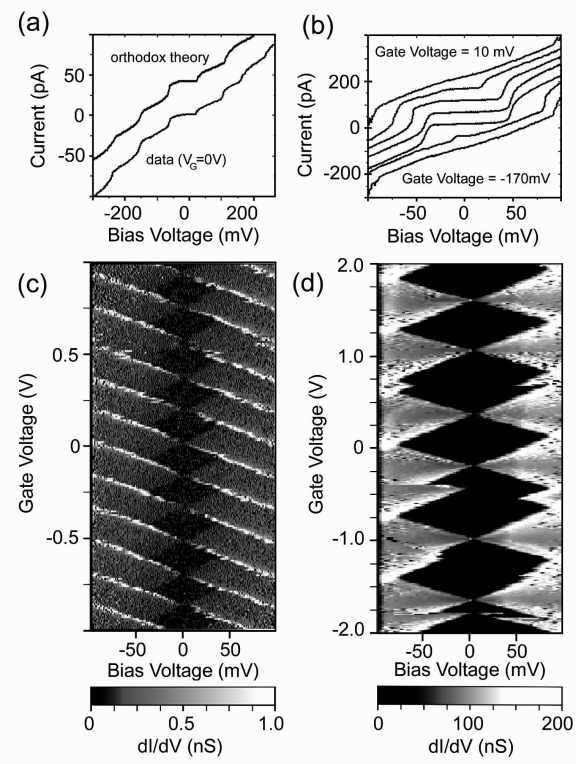


Figure 2.3: . (a) Coulomb staircase $I - V$ curve for a gold nanoparticle SET (device #1) at 4.2 K, along with an orthodox model fit (offset for clarity). (b) $I - V$ curves for device #1 at 4.2 K, for equally spaced values of V_G. (c) Gray-scale plot of dI/dV as a function of V_G and V for device #1 at 4.2 K. Eleven degeneracy points separating twelve different charge states are visible within a 2 V range of V_G. (d) Gray-scale plot of dI/dV as a function of V_G and V for device #2 at 4.2 K, showing "Coulomb diamonds" as well as several abrupt changes in the background charge of the SET island as V_G is swept.

and the source and drain capacitances are 1-10 times larger, yielding charging energies between 15 and 50 meV. As a control experiment, we took 24 devices through the full fabrication process except for the step in which the nanoparticles are deposited. These samples never showed Coulomb-blockade characteristics. In prior work, tunnel junctions containing individual metal nanoparticles have been used to measure the "electron-in-a-box" states inside the nanoparticle, and these experiments have been a rich source of information about electronic interactions within metals [8, 9]. Having a more effective gate can contribute greatly to these types of studies, by enabling investigations of how the spectra change as electrons are added to a nanoparticle, and also by giving increased control over non-equilibrium excitations [22]. Next we demonstrate that our SETs are sufficiently stable to allow measurements of the electron-in-a-box spectra, and we present initial studies of how these spectra depend on the electron number.

In order to resolve electron-in-a-box quantum states, we cool samples in a dilution refrigerator with filtered electrical lines so that the electron temperature is less than 150 mK. In Fig. 2.4 we examine a device with parameters $C_G = 2.0$ aF, $C_S = 1.9$ aF and $C_D = 2.2$ aF. Low-temperature plots of dI/dV versus V_G and V reveal a fine structure of lines beyond the tunneling threshold that correspond to tunneling via excited quantum states within the nanoparticle. Figure 2.4 shows three sets of spectra. In panel (a), the lines running parallel to the line labeled α correspond to transitions in which an electron tunnels off the nanoparticle to decrease the total number of electrons from some value N to $N-1$. Panel (b) displays a more negative range of V_G where transitions from $N-1$ electrons to $N-2$ are visible. Finally, the levels in panel (c) correspond to $N-2$ to $N-3$ transitions. The most striking aspect of these three plots is that the pattern of excited states

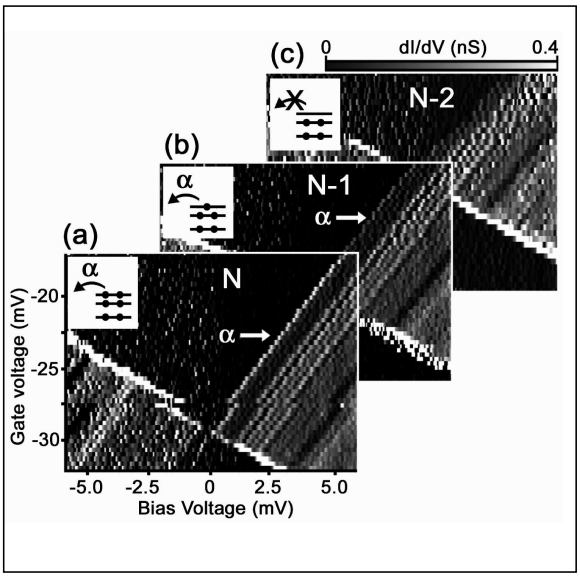


Figure 2.4: Gray-scale plots of dI/dV as a function of V_G and V, displaying the discrete electron-in-a-box level spectra within a gold nanoparticle (device #3), measured with an electron temperature less than 150 mK and zero magnetic field. Panels (a), (b), and (c) represent spectra for different numbers of electrons in the same nanoparticle. Panel (b) covers the gate voltage range from -95 mV to -110 mV and (c) the range from -180 mV to -195 mV. Insets: Energy-level diagrams illustrating the tunneling transitions that contribute to line for different numbers of electrons on the particle.

is extremely similar. The only significant difference can be seen in the line labeled α at the threshold for tunneling. In panel (a) line α is strong, in panel (b) it is present but its conductance is decreased by approximately 45%, and in (c) the line is absent. This behavior can be understood in a simple way by assuming that the energy levels in the nanoparticle are spin-degenerate, and that N corresponds to an even number of electrons. In this case, line α in panel (a) corresponds to transitions in which either one of the two (spin-degenerate) electrons in the highest occupied energy level for N electrons tunnels off of the particle into the source. For $N-1$ electrons in panel (b), one of these two electrons is already gone, so line α corresponds to having just the one remaining electron in that same energy level tunnel off of the particle. Because the source-particle interface is the rate limiting barrier in this device, the tunneling rate is reduced by approximately a factor of 2. Finally, in panel (c), no electrons are left to tunnel out of the state corresponding to line α, so the line is no longer present.

The strong similarities that we observe in the excited state spectra for different numbers of electrons on a gold nanoparticle are in striking contrast to analogous studies of GaAs quantum dots [23]. In GaAs dots, spin degeneracy is not generally observed and excited-state levels are shifted relative to one another when the electron number is changed. These spectral rearrangements in GaAs have been explained as due to exchange interactions between the added electron and quantum-dot states with different total spins. The similarity of the excited-state spectra that we observe for different numbers of electrons in gold is therefore evidence that exchange interactions are sufficiently weak that the energy levels are filled as in a non-interacting model, with each energy level spin-degenerate and with the energy-level spacings not sensitive to the electron number. This simple

outcome is highly non-trivial for an interacting-electron system, but it is consistent with expectations for the low strength of exchange interactions in gold [24].

In summary, we have fabricated single-electron transistors by depositing metal nanoparticles within break junctions made using electromigration. This method provides strong coupling between the nanoparticle and the gate electrode, thereby enabling experiments in which the number of electrons on the particle is varied over a wide range. We have demonstrated that this device geometry permits detailed measurements of electron-in-a-box level spectra in metals as a function of the electron number.

BIBLIOGRAPHY

[1] D. V. Averin and K. K. Likharev, *J. Low Temp. Phys.* **62**, 345 (1986).

[2] T. A. Fulton and G. J. Dolan, *Phys. Rev. Lett.* **59**, 109 (1987).

[3] P. Lafarge, H. Pothier, E. R. Williams, D. Esteve, C. Urbina, and M. H. Devoret, *Z. Phys. B* **85**, 327 (1991).

[4] M. J. Yoo, T. A. Fulton, H. F. Hess, R. L. Willett, L. N. Dunkleberger, R. J. Chichester, L. N. Pfeiffer, and K. W. West, *Science* **276**, 579 (1997).

[5] R. J. Schoelkopf, P. Wahlgren, A. A. Kozhevnikov, P. Delsing, and D. E. Prober, *Science* **280**, 1238 (1998).

[6] M. H. Devoret and R. J. Schoelkopf, *Nature* **406**, 1039 (2000).

[7] R. G. Knobel and A. N. Cleland, *Nature* **424**, 291 (2003).

[8] J. von Delft and D. C. Ralph, *Phys. Rep.* **345**, 61 (2001).

[9] D. C. Ralph, C. T. Black, and M. Tinkham, *Phys. Rev. Lett.* **78**, 4087 (1997).

[10] Y. A. Pashkin, Y. Nakamura, and J. S. Tsai, *Appl. Phys. Lett.* **76**, 2256 (2000).

[11] D. Davidovic and M. Tinkham, *Appl. Phys. Lett.* **73**, 3959 (1998); *Phys. Rev. Lett.* **83**, 1644 (1999).

[12] S. I. Khondaker and Z. Yao, *Appl. Phys. Lett.* **81**, 4613 (2002).

[13] M. F. Lambert, M. F. Goffman, J. P. Bourgoin, and P. Hesto, *Nanotechnology* **14**, 772 (2003).

[14] S. E. Kubatkin et al., Appl. Phys. Lett. 73, 3604 (1998); *J. Low Temp. Phys.* **118**, 307 (2000).

[15] A. Bachtold, P. Hadley, T. Nakanishi, and C. Dekker, *Science* **294**, 1317 (2001).

[16] H. Park, A. K. L. Lim, A. P. Alivisatos, J. Park, and P. L. McEuen, *Appl. Phys. Lett.* **75**, 301 (1999).

[17] As an alternative, we have also tried breaking the wires at room temperature inside the evaporator (instead of at liquid helium temperature) but this generally produced gaps too wide to make SETs with good yield.

[18] J. Park, A. N. Pasupathy, J. I. Goldsmith, C. Chang, Y. Yaish, J. R. Petta, M. Rinkoski, J. P. Sethna, H. D. Abruna, P. L. McEuen, and D. C. Ralph, *Nature* **417**, 722 (2002).

[19] W. Liang, M. P. Shores, M. Bockrath, J. R. Long, and H. Park, *Nature* **417**, 725 (2002).

[20] D. V. Averin and K. K. Likharev, in Mesoscopic Phenomena in Solids, edited by B. L. Altshuler, P. A. Lee, and R. A. Webb (Elsevier, New York 1991), p. 173.

[21] A. V. Danilov, D. S. Golubev, and S. E. Kubatkin, *Phys. Rev. B.* **65**, 65 (2002).

[22] M. M. Deshmukh, E. Bonet, A. N. Pasupathy, and D. C. Ralph, *Phys. Rev. B* **65**, 073301 (2002).

[23] D. R. Stewart, D. Sprinzak, C. M. Marcus, C. I. Duruz, and J. S. Harris Jr., *Science* **278**, 1784 (1997).

[24] D. A. Gorokhov and P. W. Brouwer, *cond-mat/0306583*.

Chapter 3

Using chemical tools to fabricate SETs

3.1 Introduction

Fillet of a fenny snake
In the cauldron boil and bake
Eye of newt and toe of frog
Wool of bat and tongue of dog
- Shakespeare

In the previous chapter we used electron beam evaporation of a metal to form an SET's island. While suitable for fabrication of test devices, this technique has several important shortcomings:

- The size of the island cannot be reliably controlled as the process of particle self assembly sensitively depends on the surface tension of metal, temperature of the substrate, and conditions of the evaporation.

- Although useful for fabricating gold devices, the technique does not scale easily to different materials.

- The nature of the tunnel barriers separating the island from the electrodes is not clear; we suspect that the barriers are formed by the layer of water molecules adsorbed on the island's surface.

We now demonstrate how this fabrication can be improved by using chemical tools to control the size, the material composition, and even the shape of the nanoparticle SET island. The material of this chapter is work in progress and as a

result rather unstructured; most of the techniques described here are unoptimized and can be further improved. We will first discuss the methods for nanoparticle synthesis and then focus on the techniques allowing positioning the nanoparticle between the source and drain electrode.

3.2 Nanoparticle synthesis techniques

The goal of this section is to offer the reader the recipes we used in synthesizing our nanoparticle devices, rather than to delve into a vast field of colloidal chemistry. Many excellent reviews on the subject [2, 3, 4] are available; the following two examples may serve well to demonstrate the power and versatility of the chemical approach:

- The size of the nanoparticle can be controlled on the atomic scale. For example, Schmid *et al.* [1] synthesized gold clusters containing precisely 55 atoms.

- By varying synthesis conditions, Ahmadi *et al.*[19] demonstrated the shape control of $\sim$ 10 nm platinum nanoparticles. The nanoparticles are either cubical, tetrahedral, or icosahedral-shaped depending on the amount of the capping agent.

The recipies we use are based on the reduction of metal salts in solution and are rather simple compared to the ones mentioned above. However, what is simple to a chemist may seem a dark magic ritual to a physicist (and certainly it did, at least to the author!), so we provide a few tips which the reader may find useful:

- Many recipes call for prolonged boiling, and large amounts of liquid can be lost in the process violating the reaction conditions. A reflux apparatus

provides a convenient solution to the problem by condensing most of the lost vapor back into the liquid state.

- Uniform heating is crucial for predictable synthesis of monodisperse nanoparticles. A flat-bottomed flask on a hotplate is not adequate for this, use a round-bottom flask with a heating tape wrapped around it.

- Many chemicals used in nanoparticle synthesis are air-sensitive and require the use of an argon glove-box. (if a chemical is hygroscopic it is probably air sensitive!). Some old glove-boxes do not have an oxygen-level gauge. In that case, use a conventional lightbulb with a broken outer shell as an oxygen indicator. If the filament burns down, there is oxygen.

- Some recipes require filtration of the final product. Normal, or gravity filtration may be excruciatingly slow process. A little vacuum on one side of the filter can speed things up significantly; a simple water pump is an ideal solution to the problem.

- Sometimes a recipe calls for a separation of two immiscible solvents (e. g. water and toluene) by using a separatory funnel. If the solvents were mixed for a long time, an emulsion which does not settle for a long time may form. In this situation, putting the solution into the refrigerator at a temperature slightly above the freezing point of either solvent may help.

- Always note the color of a nanoparticle solution. For example, a solution of gold nanoparticle larger than several nanometeres is ruby-red; a change in color towards blueish-black indicates agglomeration of the particles into larger clusters.

Using these tips and not forgetting to clean all the glassware thoroughly the nanoparticle synthesis should be fairly straightforward. In the next section we descibe the synthesis methods for both gold and palladium nanoparticles, mostly following the original recipies [5, 7, 16, 18, 17] with slight modifications.

3.3 Gold nanoparticle synthesis

Gold nanoparticles are universally used as a resolution calibration standard for electron microscopy imaging and may be purchased from the vendors such as Ted Pella, BBI international, Sigma Aldrich, Alfa Aesar. The $\sim$ 16 nm monodisperse nanoparticles can also be synthesized following the recipe of Frens *et al.* [5]:

- Prepare two soluions: Solution A ($HAuCl_4$ in water, 10^{-2}% by weight), Solution B (Na_3- citrate in water, 1% by weight). Gold tetrochloroaureate $HAuCl_4$ is extremely hygroscopic; the weighing should be done inside the glove-box.

- Heat 50 ml of solution A to boiling on a hotplate under rapid stirring (flat-bottom flask is ok), then add 1 ml of solution B.

- Within 25 s the boiling mixture starts changing color and turns red after 70 s, indicating the formation of particles. After approximately 5 minutes the reduction is completed, longer boiling does not change the size of the particle. Store the finished colloid in a dark place as nanoparticles may lose their charge and agglomerate (a change in color would indicate this) under the influence of light.

Alternatively, a wealth of recipes is available to fabricate either citrate- [5, 7] or thiolated molecules capped [9, 6, 8] monodisperse gold nanoparticle ranging in

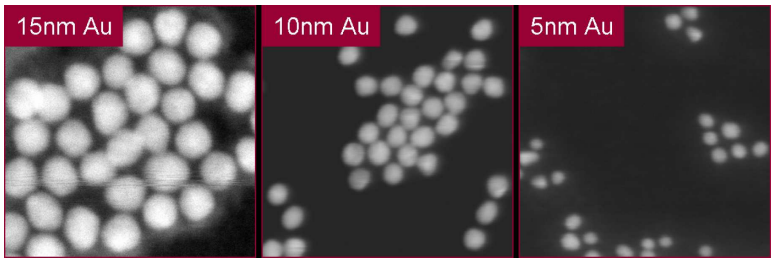


Figure 3.1: Gold nanoparticles (Ted Pella) of different sizes. The particles are highly spherical and monodisperse.

size from < 1 nm to > 150 nm.

3.4 Platinum and palladium nanoparticle synthesis

Palladium and platinum nanoparticles are interesting because of the predictions of high-spin ground states due to the strong exchange interaction in nanoscale platinum group metals [20] (see Chapter 6 for details). We use the recipe developed by Choo *et al.* [16] to synthesize Pd nanoparticles:

- Prepare solution A by adding 88.5 mg of $PdCl_2$ to 100 ml of concentrated hydrochloric acid.
- Prepare 0.832 g of polyvinylpyrrolidone with average molecular weight $M_w = 40000$ (PVP-40).
- We then add solution A and PVP-40 to a mixture of 75 ml of water and 65 ml of isopropanol. Always add acid to water!
- The solution is heated under reflux for three hours under stirring. During the refluxing we add dropwise 10ml of 0.1M $NaOH$ solution in methanol. The solution rapidly changes its color from bright-orange to black upon addition of sodium hydroxide.

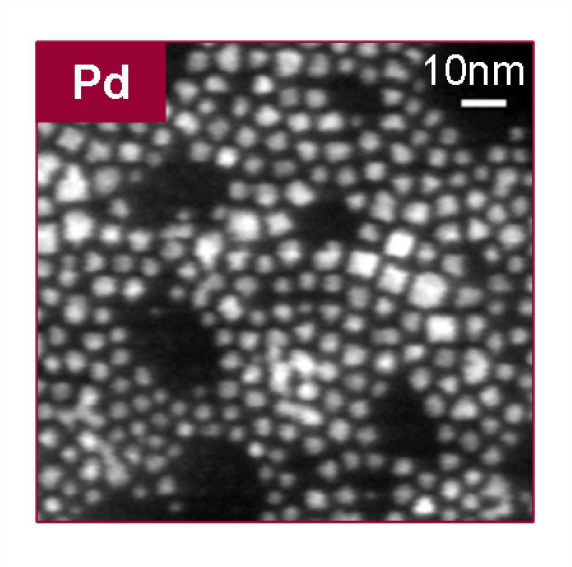


Figure 3.2: Palladium nanoparticles synthesized using the method of Choo *et al.* [16]

This recipe results in Pd nanoparticles $\sim$ 10 nm in diameter (Fig. 3.2); changing the relative amounts of PVP and Pd precursor results in size ranging from 1 to 15 nm [16].

For platinum nanoparticles we followed a modified version of the recipe by Sarathy *et al.* [17]:

- 0.5ml of 0.01 M $NaBH_4$ solution (aged for 3 hours) is mixed with 100 ml solution of 2.6 mM of H_2PtCl_6.
- Add 20 mL of 1.66 dodedanethiol solution in toluene. Stir.
- Dropwise add 1.0 ml of HCl.

The resulting nanoparticles are shown in Fig. 3.3. The particles are very polydisperse; different recipies may be used to produce monodisperse palladium nanocrystals [18].

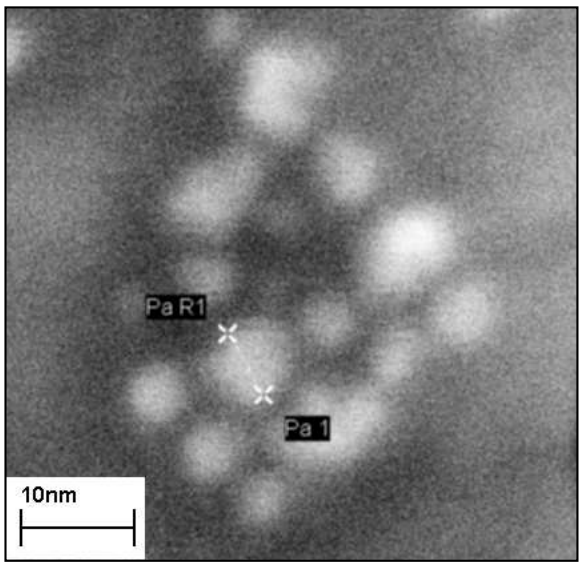


Figure 3.3: Platinum nanoparticles synthesized using the modified the method of Sarathy *et al.* [17].

Finally, a word of caution: the recipes in this section worked once and have not been reliably tested and hence should be taken with a grain of salt.

3.5 Contacting nanoparticles: molecular self-assembly

Having synthesized nanoparticles of the desired size and material composition, the next step is to incorporate them between the source and the drain electrodes to serve as the island of an SET. The most straightforward approach, placing a drop of nanoparticle solution onto a chip and letting the solvent evaporate does not work: during the evaporation particles clump together, producing a rough metallic film instead of isolated nanoparticles. Hence, the particles should be attached to the substrate while in solution; the solvent may be removed later by repeated washing. Molecular self-assembly can conveniently be used both to serve as nanoparticle "glue" and to obtain reliable tunnel barriers between the nanoparticles and the

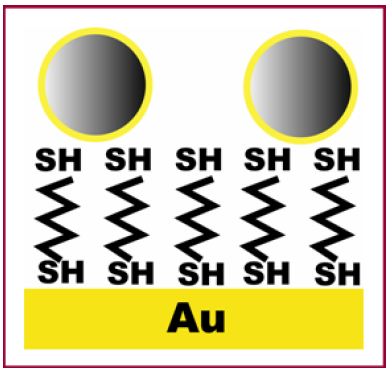


Figure 3.4: Using chemical self-assembly to place the nanoparticle onto the electrodes. A molecule with two functional endgroups may be used to attach the nanoparticle to the substrate.

electrodes.

One approach is based on self-assembly of thiolated molecules onto a metallic substrate. In a typical experiment, we first create a nanometer-sized gap between the source and the drain electrodes using electromigration at ambient temperature (see Chapter 2). We then treat the surface of the chip with a solution of molecules with functional groups (e.g. thiol $SH-$ or $NH-$ amine endgroups) on both ends. Both thiol and amine have a high affinity towards gold [3], and molecules form a dense self-assembled monolayer on the surface of the electrodes. We then place the device into a nanoparticle solution and the second endgroup of the functional molecule attaches itself to the nanoparticle resulting in the assembly of a layer of nanoparticles on the electrodes (Fig. 3.4). Finally, we measure the resistance between source and drain electrodes and wirebond the devices which changed their resistance after the assembly, indicating the presence of a nanoparticle between the electrodes.

The following recipe (due to Sato *et al.* [10]) results in a self assembly of gold

nanoparticles on both gold electrodes and silicon or aluminum oxide:

- First, the electrodes are prepared for self-assembly and cleaned from contaminants and residue of e-beam resist. Typically, we clean the electrodes using an oxygen plasma asher (e.g. RIEX, Pressure: 30 mT O_2, Power: 100%, Flow: 30, Time: 3 min). Although it is normally chemically inert, gold tends to oxidize in the presence of an oxygen plasma [24]. Hence, we remove gold oxide by treating the chip with ethanol for at least 20 minutes right after the plasma cleaning.

- We then transfer the chip into 0.05% (volume/volume) water solution of 3-(2-aminoethlyamino)propyltrimethoxysilane (APTS) for 10 minutes; the main safety concern here is not to break your tongue when trying to pronounce the name of this chemical.

- After APTS immersion we rinse the sample in DI water and then put it into a 120 C° oven. The ATPS treatment replaces the OH group on the substrate with the APTS molecule. The amino group on the end of the molecule is oriented away from the surface.

- Finally, we transfer the chip into water solution of gold nanoparticles. Due to its high affinity to gold [3], the amine group may bind to a nanoparticle, immobilizing it on the substrate. The acidity of the solution is adjusted to $pH \sim 3$ using citric acid buffer. The final step is rather slow; we typically leave in the chip in the solution for at least 24 hours.

Adjusting the acidity of the solution in the last step of the recipe is important; Figure 3.5(a) shows that a solution with $pH \sim 6$ (which is the acidity of the nanoparticle solution synthesized following Frens *et al.* [5]) results in a very low

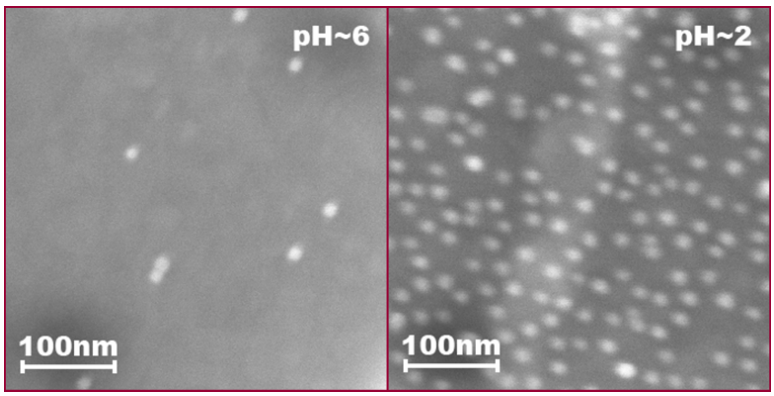


Figure 3.5: The acidity of the gold nanoparticle solution can be adjusted to control the surface coverage of the nanoparticles.

density coverage of the nanoparticles. Of course, the surface density should be increased in order to obtain a reasonable yield of working devices.

To understand how acidity affects the coverage, we need to examine process of the self-assembly and its key element, the electrostatic interaction between nanoparticles and amine groups of the molecules attached to the substrate. Gold nanoparticles carry a negative charge due to the adsorption of anions [25]. Amine groups of the functional molecule, on the other hand, are positively charged at low pH due to partial protonation. As a result, the nanoparticles are electrostically attracted towards the amine groups and stick to the surface. The density of the nanoparticle layer is then determined by the Coloumb repulsion between the neighboring nanoparticles; the process of self-assembly stops when the surfaces charges of the amine groups and nanoparticles balance each other.

The effective charge of the nanoparticles can be controlled by means of tuning the pH of solution [12]. At $pH \sim 2$ nanoparticles "fall out" of solution (the solution turns first blue and then the black, black residue appears at the bottom), indicating the nanoparticles are neutral and that the Coulomb repulsion is absent. At slighly

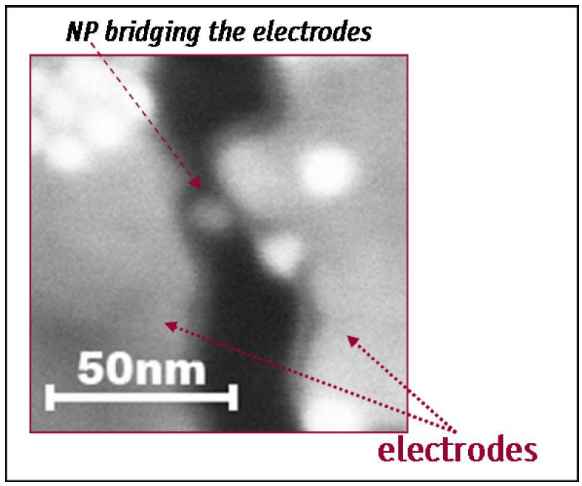


Figure 3.6: Gold nanoparticle between two electodes resulting in a stable single electron transistor

higher pH values particles bear a small negative charge, while the amine groups are still positive; as a result the nanoparticle surface coverage increases dramatically (Fig. 3.5(b)). This, in turn, leads to a higher yield of working devices, such as the device in Fig. 3.6.

Different versions of the recipe by Sato *et al.* use the molecules with thiol [12, 13] or amine endgroups [10, 11] in either water-based [10, 11, 12, 13] or ethanol-based solvents. The nanoparticles can be assembled either on gold, aluminum, aluminum oxide or silicon oxide.

The devices formed via chemical self-assembly (e.g. the device in Fig. 3.6) are stable enough to resolve particle-in-a-box states at milliKelvin temperatures. Figure 3.7 shows the conductance as a function of gate and bias voltage for a device with a 15 nm gold nanoparticle serving as an island of the SET and APTS tunnel barriers. Particle-in-a-box levels are clearly resolved; the level spacing $\delta =$ 0.07 meV extracted from the data is in close agreement with the free-electron estimate Eq. (1.8) for a spherical gold particle of the same size. The yield of

useful devices is fairly high (about 10 out of 36 lines change their conductance after the self-assembly, about 2-3 devices exhibit a clear spectrum of particle-in-a-box states) making the technique appropriate for electron level spectroscopy experiments. We are now at the very initial stages of experiments with chemically synthesized devices; chemical control, however, opens a door to studying a number of exciting topics:

- The influence of the exchange interaction on electron level filling of Pt-group metallic or ferromagnetic nanoparticles (more on this in the last chapter).
- The influence of controlled disorder [28] in the nanoparticle on the distribution of g-factors.
- The structure of the electronic level spectra in frustrated magnets [30] and antiferromagnets [31].
- The structure of the electronic level spectra in the quantum dot "molecules" [29].

Before starting these or other experiments it is important to implement one improvement to the present fabrication technique: We used a silicon backgate device design [26] for the chemically self-assembled devices, as the acidic nanoparticle solution seem to damage the aluminum oxide gate. Although dispersing the nanoparticles in the non-polar solvent such as toluene or hexane might help, further work is required to find a combination of nanoparticles and solvents compatible with aluminum oxide gates.

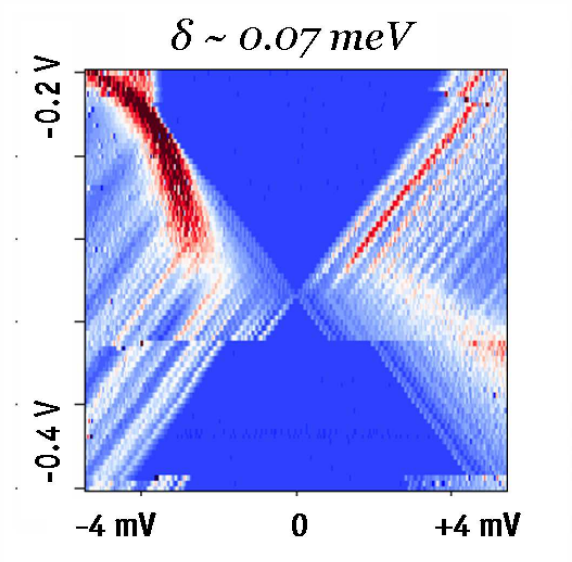


Figure 3.7: Conductance (colorscale) as a function of bias and gate voltages for a chemically synthesized metallic nanoparticle SET. The island of the SET is a 15 nm gold nanoparticle (Ted Pella), APTS molecules bind the particle to the electrodes.

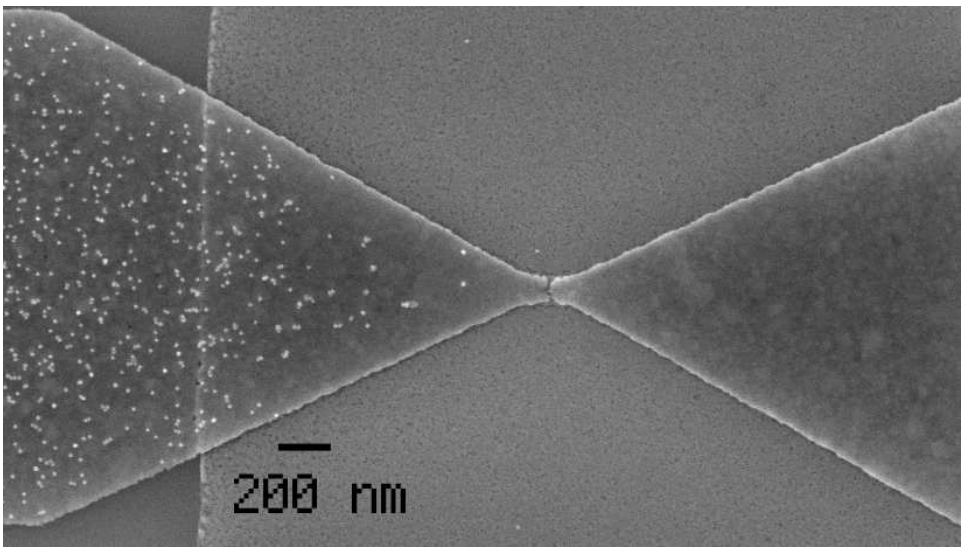


Figure 3.8: Gold nanoparticles are only deposited onto the electrode kept at the positive bias (on the left).

3.6 Alternative approaches to self-assembly

We have explored several alternative pathways for assembling nanoparticles onto the surface of the electrodes. Two examples of such methods are electrophoretic deposition (e.g. [14]) and electrostatic trapping [15, 22, 23].

Dielectrophoresis makes use of the nanoparticles' slight negative charge in solution; constant electric field is employed to drive the particles towards the electrodes. In a typical experiment, we place a small beaker with solution into the probe station and positively bias the electrodes (typically $\sim$ 800 mV for $\sim$ 2 min) with respect to a reference platinum electrode. For the sample shown in Fig. (3.8) we biased only the electrode on the left. An SEM image taken after the self-assembly indicates a high density of the nanoparticles on this left electrode, while we see no particles deposited on the right electrode.

Electrostatic trapping makes use of a metallic object's dipole attraction towards

the gradient of an electric field to position a nanoparticle between the electrodes. The original method was developed by Bezryadin *et al.* [15] and perfected by Krahne *et al.* [22] and Amlani *et al.* [23]: First, two electrodes spaced several nanometers are fabricated, and a drop of solution is dispensed on top of the gap between the electrodes. Then, a voltage is applied across the gap to produce a gradient of the electric field. Once the particle is bridging the gap the voltage drop across the gap is reduced due to the presence of a series resistance and no further particles are attracted.

However, in electrochemist's eyes this recipe is nothing short of a complete blasphemy:

- Water solution of sodium citrate (in which the particles are suspended) is an excellent electrolyte. When the applied voltage exceeds the so-called electrochemical window of water (several hundered mV), gas starts to evolve from one of the electrodes, metal ions are deposited on the other. Abundant artifacts are expected as a result [27].

- As-prepared nanoparticle solution is reasonably conductive and should screen the potential of the electrodes. The electrotrapping is expected to be much less effective compared to naive electrostatic estimates.

- It would seem that applying an oscillating AC voltage instead of DC should solve both of the previously mentioned problems once the oscillation frequency exceeds the "plasma frequency" of ions in the solution. However, the "plasma frequency" is in the GHz range [21] and hence out of our reach.

Two modifications of the original recipe may help to minimize the problems: The solutions needs to be as ion-free as possible and the volume of the solution should

be as little as feasible. This is how we go about it:

- Metal ions can be removed from the solution using dialysis. Pour the solution into a dialyzer tube, put the tube into a large (several liters) beaker with clean DI water and leave it stirring overnight. Repeat several times. The presence of ions can be monitored using a water conductance meter.

- Drops as small as 0.3 μL (yes, microliters!) can be dispensed using *Pippeteman* pippets. However, such small drops evaporate in minutes making the electrotrapping impossible (A drop covers one die with 6 devices; electrotrapping time is $\sim$ 2 min. per device.) To improve the lifetime, before depositing the drop we cool down the chip using a small Peltier cooler. Maintaining the temperature of the chip at 4 C° can extend the lifetime of a drop to over 40 minutes.

With all mentioned considerations in mind we developed the following modified recipe:

We first place the chip under the probe station and create gaps between the electrodes using electromigration as described in the second chapter. Using a micropippete we place a drop of $\sim$0.3 μL of the gold nanoparticle solution (dialized to remove ions) on top of the prepared electrodes at the substrate temperature 4 C°. We then contact the source and the drain electrodes using the probe station and apply AC voltage $\sim$ 800 mV, 1 MHz using a series resistor $>$ 100 kΩ. After several minutes we wash the chip with DI water and measure the change of resistance between the electrodes. Some of the device exhibit a large decrease in resistance and nanoparticles can sometimes be seen bridging the electodes (Figure 3.9).

We have only tried this recipe a couple of times and the SEM of Fig. 3.9

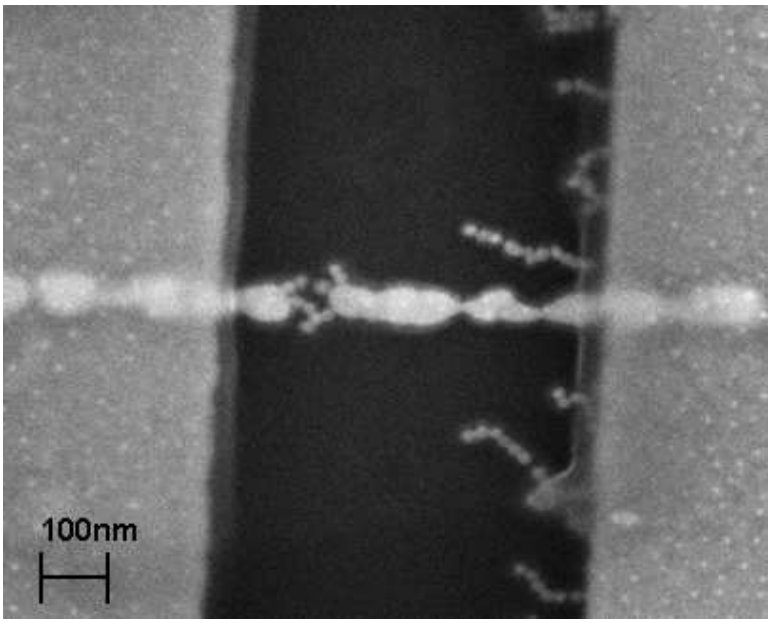


Figure 3.9: Gold nanoparticles are placed between the electrodes using electrostatic trapping.

is the best we have; so far no devices have been found to exhibit a clear SET behaviour. However, electrotrapping seems to hold a promise as a method of choice for nanoparticle SET fabrication since the method is not sensitive to the particulars of the SAM chemistry and may potentially be applicable to any combination of electrodes/nanoparticle materials.

BIBLIOGRAPHY

[1] G. Schmid *et al.*, *Chem. Ber.* **114**, 3634 (1981).

[2] G. Schmid, *Chem. Rev.* **95**, 1709 (1992).

[3] A. N. Shipway, E. Katz, I. Willner, *Chem. Phys. Chem* **1**, 18 (2000).

[4] B. L. Cushing, V. L. Kolesnichenko, and C. J. O'Connor, *Chem. Rev.* **104**, 3893 (2004).

[5] G. Frens, *Nature* **241**, 20(1973).

[6] D. V. Leff, P. C. Ohara, J. R. Heath, and W. M. Gelbart, *J. Phys. Chem* **99**, 7036 (1995).

[7] K. Turkevich, J. Hillier, P. C. Stevenson, *Disc. Farad. Soc.* **11**, 55 (1951).

[8] M. J. Hostetler, *Langmuir* **14**, 17 (1998).

[9] M. Brust, J. Fink, D. Bethell, D. J. Schiffrin, and C. Kiely, *J. Chem. Soc. Chem. Commun.*, 1655 (1995).

[10] T. Sato, D. G. Hasko, and H. Ahmend, *J. Vac. Sci. Technol. B* **15**, 45 (1997).

[11] T. Sato, D. Brown, and B. F. G. Johnson, *Chem. Comm* 1007 (1997).

[12] T. Zhu, X. Fu, T. Mu, J. Wang, and Z. Liu, *Langmuir* **15**, 5197 (1999).

[13] J. Wang, T. Zhu, M. Tang, S. M. Cai, and Z.F. Liu, *Jpn. J. Appl. Phys.* **36**, L1381 (1996).

[14] M. Giersig and P. Mulvaney, *Langmuir* **9**, 3408 (1993).

[15] A. Bezryadin, C. Dekker, and G. Schmid, *Appl. Phys. Lett.* **71**, 1273 (1997).

[16] H. P. Choo, K. Y. Liew, W. A. K. Mahmood, and H. Liu, *J. Mater. Chem.* **11**, 2906 (2001).

[17] K. V. Sarathy, G. Raina, R. T. Yadav, G. U. Kulkarni, and C. N. R. Rao, *J. Phys. Chem. B* **101**, 9876 (1997).

[18] J. Yang, J. Y. Lee, T. C. Deivaraj, H.-P. Too, *J. Coll. Int. Sc.* **277**, 95 (2004).

[19] T. S. Ahmadi, Z. L. Wang, T. C. Green, A. Henglein, M. A. El-Sayed, *Science* **272**, 1924 (1996).

[20] P. W. Brouwer, Y. Oreg, and B. I. Halperin, *Phys. Rev. B* **60**, 13977 (1999).

[21] Hector Abruna and Jacob Grose, *private communication.*

[22] R. Krahne *et al.*, *Physica E* **17**, 498 (2003).

[23] I. Amlani, A. M. Rawlett, L. A. Nagahara, and R. K. Tsui, *Appl. Phys. Lett* **80**, 2761 (2002).

[24] R. F. Carvalhal, R. S. Freire, L. T. Kubota, *Electroanalysis* **17**, 1251 (2005).

[25] D. Thompson and I. Collins, *J. Colloid Interface Sci.* **152**, 197 (1992).

[26] A. Pasupathy, *Ph. D. Thesis* (2004).

[27] J. E. Grose, A. N. Pasupathy, D. C. Ralph, B. Ulgut, and H. D. Abruna, *Phys. Rev. B* **71**, 035306 (2005).

[28] S. Link, Z. L. Wang, and M. A. El-Sayed *J. Phys. Chem B*, **103**, 3529 1999.

[29] T. Dadosh, Y. Gordin, R. Krahne, I. Khivrich, D. Mahalu, V. Frydman, J. Sperling, A. Yacoby, and I. Bar-Joseph, *Nature* **436**, 677 (2005).

[30] S. Sun, C. B. Murray, D. Weller, L. Folks, A. Moser, *Science* **287**, 1989 (2000).

[31] S. D. Tiwari and K. P. Rajeev, *Phys. Rev. B* **72**, 104433 (2005).

Chapter 4

Understanding the properties of nanometer-sized magnetic electrodes

4.1 Introduction

Oh no! Not the magnet!

- Bender

In order to realize the ferromagnetic SET described in the first chapter, we need to fabricate a pair of ferromagnetic electrodes separated by a tunneling gap and to separately control the magnetization direction of the electrodes (Fig. 1.4(b)). On the surface, this appears an easy task: just like before, we can use electromigration to fabricate a gap in a ferromagnetic wire and apply an external magnetic field to rotate the magnetization of the electrodes.

This approach was taken by Pasupathy *et al.* [15]; the authors used differently shaped electrodes to produce different switching fields for the source and the drain. Nickel electrodes were used to contact a single fullerene molecule in order to study the coexistence of the Kondo effect and ferromagnetism. However, in the design of Pasupathy *et al.* the angle between the magnetization vectors of the electrodes cannot be controlled reliably: Micromagnetic simulations show that the angle is dependent on the small-scale features of the electrodes' surfaces and is typically smaller than 30°. Also, even without the molecule bridging the electrodes, the magnetic properties of the system are not well understood: For example, the tunneling magnetoresistance ratio, which should reflect polarization of the electrons at the Fermi level, varies between different devices and in some cases even changes

its sign.

Building on the work of Pasupathy *et al.*, we started experiments designed to improve the design of magnetic electrodes. In particular, our goals were:

- to explore the difference between magnetoresistance in nanometer-sized ferromagnetic contacts and the better-understood case of bulk ferromagnets.
- to reliably control the angle between magnetization direction of the source and the drain electrodes of ferromagnetic SET.
- to find materials yielding predictable high values of magnetoresistance in nanoscale ferromagnetic tunneling junctions.

Along the way, we came to realize that the problem of understanding magnetotransport in nanometer-scale ferromagnetic devices has much broader implications. Nanoscale ferromagnetic spin-valves are considered a likely candidate for future magnetic random access memory, promising fast readout, nonvolatility, and low energy consumption. The information in such a MRAM is encoded in the direction of the magnetization of one of the electrodes, and read out using magnetoresistance effects. Of course, the larger MR ratio is the faster and the more reliable the read-out can be made.

Several years ago reports started to appear [6, 7] of magnetoresistances exceeding 1000% in different setups featuring atomic-scale ferromagnetic contacts. These experimental results were interpreted as a consequence of a magnetic domain wall entering the constriction and contributing to the anomalous scattering of the electrons [4]. Many argued that if controllably reproduced, the effect (named BMR, or ballistic magnetoresistance) could lead to a new generation of magnetic memories. Several groups [13, 10] have tried to reproduce the BMR effect in different better-

controlled geometries, but observed no trace of high MR. Moreover, some workers [10, 8] traced the appearance of resistance changes to the mechanical motion of the electrodes due to magnetomechanical effects, leading to significant controversy.

As we will see, one of the main reasons for the controversy was a lack of experimental techniques to fabricate atomic-scale ferromagnetic contacts rigidly attached to the substrate. Much to our surprise, controlled electromigration on a ferromagnetic wire (very similar to the method used in Chapter 2 for gold wires) turned out to be a near-ideal solution to the problem. Hence, the experiments described in this chapter were extended to examine the possibility of the anomalous electron scattering off an atomically-sharp domain wall. Here, we describe our initial effort which yielded more questions than answers; the angle-resolved magnetoresistance measurements in the next chapter help to establish a clearer picture.

4.2 Domain walls in narrow ferromagnets: contribution to the resistance

Let us now briefly consider how domain walls may influence electronic transport in a ferromagnet. Normally, the only contribution of the domain wall to a ferromagnet's resistance arises due to AMR effect as the magnetization direction (described by the angle $\theta(x)$ of the magnetization vector) at the location of the wall differs from the magnetization in the rest of the ferromagnet (Fig. 4.1). The small size of the AMR effect results in very small resistance change ($\Delta R/R < 1$ %) when a domain wall is formed. For a metallic ferromagnet the typical width of a domain wall (e.g. ~ 70 nm in Nickel) is much larger than the Fermi wavelength λ_F ($\lambda_F < 1$ nm), and electrons can adiabatically adjust to the magnetization direction,

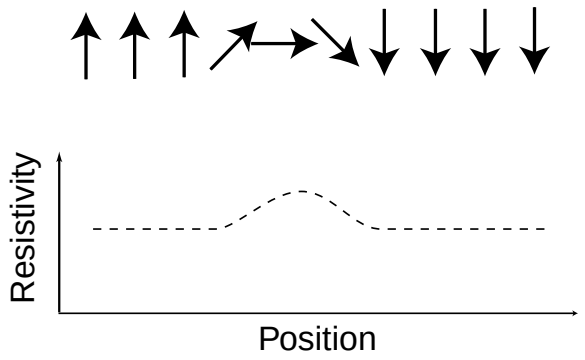


Figure 4.1: Domain wall contributing to ferromagnet's resistance due to AMR.

and get transmitted across the domain wall without scattering. This situation may change for a ferromagnet which has a constriction which is narrow on the scale of the bulk domain wall width w. As we will now see, in such constrained geometry the width of the domain wall is determined by the size of the constriction, rather than by the bulk properties of the ferromagnet. In that case the potential due to the wall is no longer uniform on the scale of λ_F and electrons may be scattered by the wall's potential. Careful theoretical analysis [4, 24] confirms this scenario, predicting a large change of conductance (more than 400% in [24]) due to the presence of a domain wall inside a chain of ferromagnetic atoms.

To understand how such atomically-narrow domain wall may come about, we follow the arguments due to Bruno [3]. Let us consider a homogenous ferromagnetic contact with the easy axis z and the cross-section area $S(x)$ exhibiting a minimum around $x = 0$ (postition of the constriction). As we will see, in order to minimize its energy, the domain wall gets localized near that constriction. We assume that magnetization of the wall depends on x only and can be described by one parameter $\theta(x)$. Let's also assume that the ferromagnet is characterized by the exchange stiffness A and an uniaxial anisotropy $F(\theta) = Kcos^2(\theta)$ [1]. We then can easily

write down the free energy of the ferromagnet:

$$E = \int_{-\infty}^{+\infty} (A\theta^2 + F(\theta))S(x)dx \tag{4.1}$$

The structure of the wall may be obtained by solving the corresponding Euler equation

$$\theta'' + \theta' \frac{S'}{S} - \frac{F'(\theta)}{2A} = 0, \tag{4.2}$$

subject to the boundary conditions $\theta(\pm\infty) = \pm\pi/2$. The second term in this expression vanishes for homogenous ferromagnets, and the equation can be easily solved. Defining the width of the wall as

$$w = 4\left[\int_{-\infty}^{\infty} \theta'^2(x)dx\right]^{-1}, \tag{4.3}$$

for a homogenous ferromagnet we obtain $w = 2\sqrt{A/K}$, a familiar textbook expression [1]. For a ferromagnet with coordinate-dependent profile S(x) the equation (4.2) can be solved analytically for certain simple profiles. For example, for a profile $S(x) = S_0(1 + \frac{x^2}{d^2})$ the expression (4.3) yields $w = 8d/\pi^2$. Surprisingly, the width of the wall is now determined by the width d of the narrowest part of contact, rather than by material properties such as the exchange stiffness A or the anisotropy K. This observation is rather general, one may show that the width of the domain wall is determined by the width of the narrowest part of constriction for an arbitrarily shaped ferromagnet [3].

Thus, in atomically narrow ferromagnets the width of the domain wall may become comparable to the Fermi wavelength scale which in turn may result in anomalous scattering of the electrons and decreased conductance [4].

4.3 Prior work: the mystery of 1000% magnetoresistance

Atomic-sized ferromagnetic contacts may be fabricated using a variety of approaches:

Spin-polarized STM [22] A ferromagnetic STM tip may be used to inject spin-polarized electrons into a ferromagnetic substrate. A rapidly oscillating magnetic field is applied to modulate the magnetization direction of the tip but not of the substrate; the magnetoresistance ratio can be measured by analyzing the component of the tunneling current at the modulation frequency. The approach allows mapping the magnetoresistance as a function of both tip-substrate separation and of the tip position.

Ferromagnetic mechanical breakjunction [6] The approach allows examining both the regimes of metallic transport in atomic sized contacts and tunneling across atomic-sized gap. The contacts are fabricated by slowly pulling on a notched ferromagnetic wire, while monitoring both the magnetoresistance and the resistance of the wire (to estimate the cross-section of the contact). The pulling is typically performed in vacuum, to avoid oxidation of the ferromagnets.

Electrodeposited ferromagnetic contacts [7] In this setup, one starts with two nickel wires separated by a gap several microns across. A potential difference is then applied between the wires while they are submerged in electrolyte solution to electrochemically deposit metal into the gap. The deposition is stopped when the resistance of the gap drops to a preset value, determining the width of the bridge connecting the electrodes.

Large MR ratios were reported in both ferromagnetic mechanical breakjunctions ($\Delta R/R \sim 200\%$ [6]) and in electrodeposited atomic-sized contacts ($\Delta R/R \sim 100,000\%$ [7]). However, these results were hard to reproduce, and other workers did not observe any enhanced contribution in better-controlled experiments [13, 14], which, however, did not reach the near-atomic size of the contacts. To add to the confusion, Egelhoff *et al.* pointed out that the anomalous change in resistance in the experiments of Garcia *et al.* [6] and Hua *et al.* [7] may result from magnetic field induced change of the contacts' shape.

Let us review the arguments of Egelhoff *et al.* in more detail. It is well known that ferromagnets tend to change their shape when magnetized due to magnetostriction [1]. For example, a nickel cylinder contracts by factor of approximately $\sim 60 \times 10^{-6}$ when a magnetic field large enough to saturate the magnetization is applied along the axis of the cylinder. While negligible in most macroscopic measurements, the effect of the contraction may have dramatic effects on the tunneling current between two ferromagnets. A nanometer-sized gap in a suspended millimeter-long nickel wire may change by a factor of 60 upon the rotation of magnetic field, resulting in the complete suppression of the tunneling current and a near-infinite apparent magnetoresistance. The electrodeposited contacts may also be susceptible to magnetostriction [10]: their structure is known to consist of networks of loosely connected grains which may expand or contract when magnetic field is applied. The resulting change in conductance may also mimick the magnetoresistace.

To avoid these artifacts of mechanical instabilities and achieve reliable measurements of the intrinsic magnetoresistance of atomic-scale magnetic contacts, we argue that at least three conditions should be met:

- the magnetic electrodes should be attached rigidly to a non-magnetic substrate with no suspended parts, so that influences of magnetostriction and magnetostatic forces are minimized.

- the measurements should be performed at cryogenic temperatures so that the contact region is thermally stable (even at a fixed magnetic field, room temperature contacts are typically unstable on time scales of seconds [9]).

- the geometry of the magnetic electrodes should be designed so that their moments can be controlled between reliably antiparallel and parallel configurations.

In the next section, we describe the experiments which fulfill all three conditions for contact sizes down to the atomic scale. This for the first time allows a reliable examination of the magnetic domain wall contribution to magnetoresistance in atomic-scale contacts in a geometry which minimizes the influence of magnetomechanical artifacts.

4.4 Fabrication

In this section we discuss the fabrication of two thin-film ferromagnets connected by a small magnetic constriction which can be controllably narrowed by electromigration from about 100 $\times$ 30 nm^2 to the atomic scale and finally to a tunnel junction. This allows us to study the MR as the contact region between the two ferromagnets is progressively narrowed in a single sample. One advantage of this device geometry is that the magnets are attached rigidly to a non-magnetic substrate with no suspended parts, so that the influence of magnetostriction and magnetostatic forces on the contact are expected to be negligible. Two previous

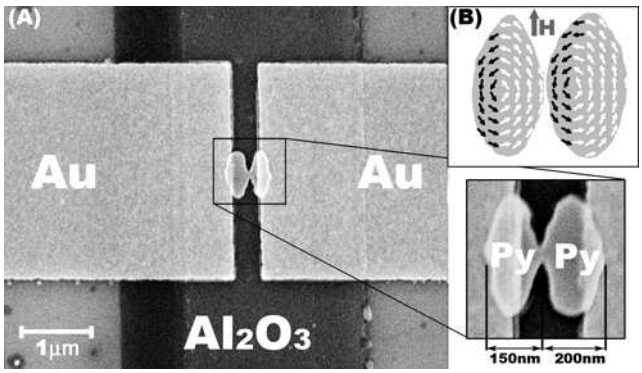


Figure 4.2: (a) Scanning electron micrograph of a finished device. Gold electrodes are used to contact two permalloy thin-film magnets (inset) on top of an oxidized aluminum gate. The irregular shape of the Py electrodes results from imperfect liftoff during fabrication. (b) Micromagnetic modeling showing antiparallel magnetic alignment across the tunneling gap in an applied magnetic field of H= 66 mT.

experiments have also achieved mechanically-stable magnetic devices for MR studies by means of nanopores and ion milling techniques [13, 14], but these devices were not tunable to near the atomic scale.

In the design used here (shown in Fig. 4.2) the electrodes are elongated along the axis perpendicular to the constriction that connects them. A magnetic field is applied parallel to the long axis of the electrodes. From simple magnetostatic considerations one expects that dipole interactions between the two electrodes will favor AP alignment with a domain wall in the constriction region for small applied magnetic fields. For sufficiently strong applied fields, both moments align parallel (P) to the field. We have performed micromagnetic modeling of this geometry using the OOMMF code [16]. We find that the electrodes can access some states other than the simple uniform P and AP states at intermediate values of field (see the vortex states in Fig. 4.2(b), but the local magnetizations on opposite sides of

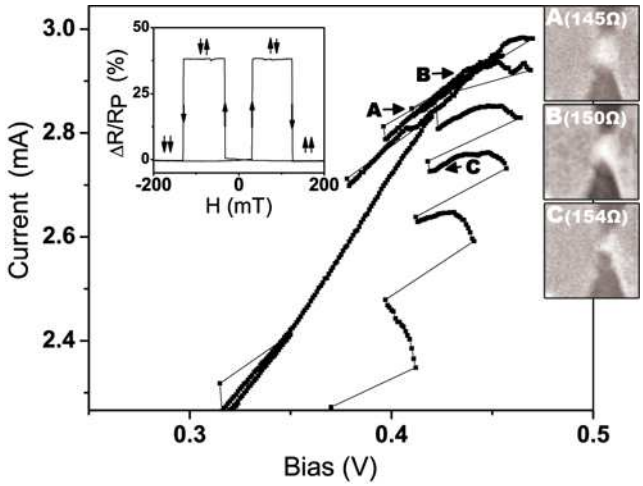


Figure 4.3: The cross section of a constriction is reduced in stages (a,b,c) by repeatedly ramping the bias voltage until electromigration begins, and then quickly decreasing the bias, following a procedure similar to that in [18]. The SEM micrographs illustrate the gradual narrowing of the constriction, which appears bright in these images. Inset: Resistance as a function of magnetic field for a tunneling device exhibiting abrupt switching between parallel and antiparallel magnetic states.

the constriction region still accurately remain either P or AP. When the electrode magnetizations are AP and they are connected by a narrow bridge of ferromagnetic metal, a domain wall forms inside the bridge. We expect that the rotation of the magnetization within the domain wall occurs in plane of the thin-film electrodes, since the demagnetization field of the film will prevent the formation of a Bloch wall. However, the detailed structure of the domain wall is expected to depend on the atomic arrangement in the bridge connecting the two ferromagnets [12].

We fabricate the devices on top of an oxidized aluminum gate electrode (not used in this experiment), on a silicon substrate by using aligned steps of electron-beam lithography [17] and thermal evaporation to first deposit gold contact pads

20 nm thick and then the magnetic permalloy electrodes 30 nm thick, with a 100 nm wide permalloy bridge connecting the magnetic electrodes (Fig. 4.2(a)). We chose permalloy for its low crystalline anisotropy, low magnetostriction and high spin polarization at the Fermi level.

To vary the size of the bridge connecting the two magnetic electrodes, we use controlled electromigration [18] at liquid helium temperatures. We slowly ramp the voltage across the constriction while monitoring the current. At roughly 3 mA (10^8 A/cm^2), electromigration begins (as indicated by an increase in differential resistance), at which point the acquisition software quickly lowers the bias. Repeating this procedure allows us to increase the resistance of the junction to any desired value between 100 Ω and 1 kΩ with better than 10% accuracy and to values between 1 kΩ and 20 kΩ with better than 50% accuracy.

We have imaged the process of controlled electromigration inside a scanning electron microscope using test samples at room temperature. Fig. 4.3 (a,b,c) shows the gradual narrowing of the constriction as electromigration proceeds, and demonstrates that electromigration produces a single break near the narrow region of the permalloy bridge. Once the permalloy constriction becomes narrower than about 10 nm, its structure cannot be resolved in the SEM. Devices for which electromigration is allowed to proceed to form a tunneling gap exhibit magnetic tunnel-junction characteristics (Fig. 4.3, inset), with stable switching between well-defined P and AP states. This agrees well with the micromagnetic simulations.

4.5 Measurements

We perform transport measurements at 4.2 K with the samples either immersed in liquid helium or in cryogenic vacuum, to minimize the possibility of oxidation

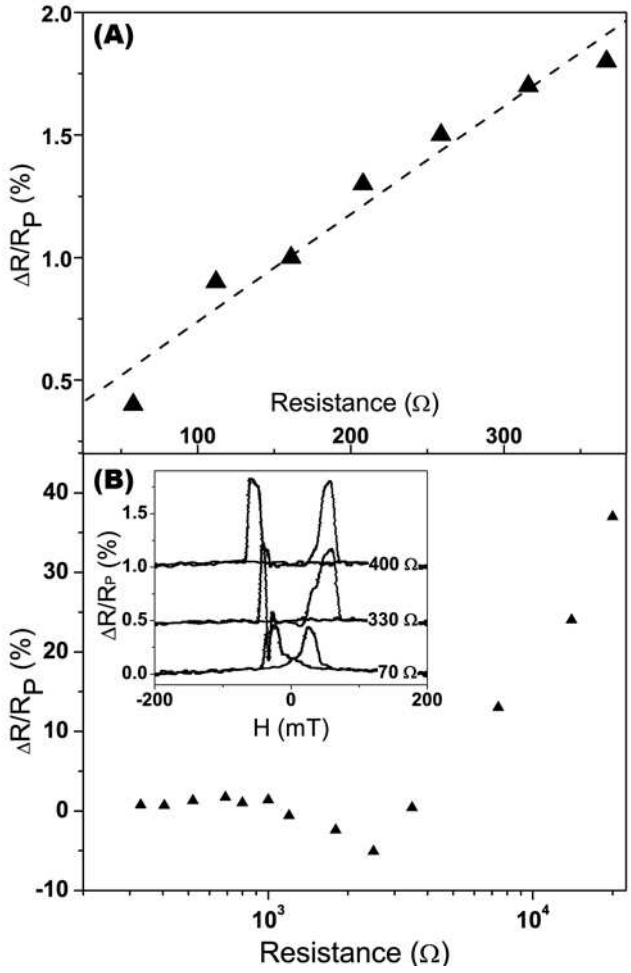


Figure 4.4: (a) Magnetoresistance as a function of resistance in the range less than 400 Ω (device I). (b) Magnetoresistance as a function of resistance in the range 60 Ω - 15 kΩ (device II). Inset: Switching behavior of device II at different resistances (curves are offset vertically for clarity.)

during and after the electromigration process. Initially, the resistance of each 100 nm wide device is approximately 60 Ω. The constriction between magnetic electrodes is then progressively narrowed by electromigration, with magnetoresistance measurements made after each stage. When the resistance begins to approach a significant fraction of $h/e^2 = 25.8\ k\Omega$, the transport is likely to be dominated by ballistic transport through just a few apex atoms. Finally, for devices with resistances of more than approximately h/e^2 the transport is dominated by electron tunneling. We find that the MR properties of the devices are qualitatively different in the regimes of low resistance (< 400 Ω), intermediate resistance (400 Ω - 25 kΩ) and tunneling (> 25 kΩ), so that we will analyze these regimes separately below.

When the resistance of a device is low (< 400 Ω) it increases smoothly as electromigration proceeds. The cross-section of the constriction varies from 100 × 30 nm^2 (60 Ω) to approximately 1 nm^2 (400 Ω), with the latter estimate based on the Sharvin formula [19]. In this regime we find small (< 3%) positive MR which increases as the constriction is narrowed (Fig. 4.4(a)). This is consistent with other recent experiments [13, 20] and well described by the semiclassical theory due to Levy and Zhang [4]. In this theory, the resistance of the domain wall scales inversely with its width and the MR ranges typically from 0.7% to 3% for bulk ferromagnets.

The resistance range from 400 Ω to 25 kΩ corresponds to a crossover between ballistic transport through just a few atoms and tunneling. In this regime the resistance of the device increases in discrete steps during electromigration and the process is less controllable. Similar behavior is seen in conventional mechanical break junctions and corresponds to the rearrangement of atoms in the constriction [21]. In this intermediate regime, the value of MR exhibits pronounced dependence

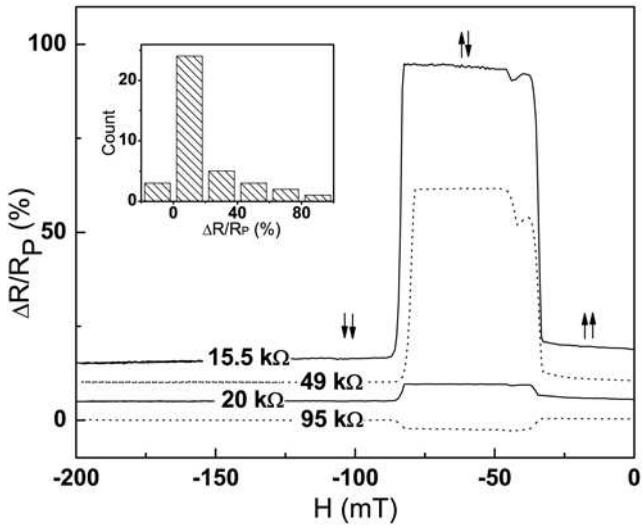


Figure 4.5: The evolution of magnetoresistance in the tunneling regime (device III) as the resistance of the tunneling gap is changed by electromigration (curves are vertically offset for clarity). Inset: distribution of magnetoresistances for devices in the tunneling regime (> 20 kΩ).

on the resistance of the device. The MR has a minimum for resistances above 1 kΩ, and typically changes sign here to give negative values. As the resistance is increased further into the kΩ range, the MR increases gradually to positive values of 10-20%. These trends are reproducible, although the exact dependence of the MR on resistance differs from device to device. The highest MR that we have observed was 80% for a device with a resistance of 14.5 kΩ. The MR values that we observe in the point contact regime are smaller than expected from scaling results of the semiclassical theory [4]. This difference is not surprising when the current is transmitted through just a few quantum channels [12]. The MR curves for all of the samples in the metallic regimes, with resistances below h/e^2, do not exhibit abrupt transitions between the P and AP resistances when the magnetic field is swept, but rather show more gradual and irregular behavior (Fig. 4.4(b),

inset). The form of the MR curve also varies as a device's resistance is increased. This suggests that the position and structure of the domain wall in the constriction may change as the magnetic field is varied.

When the resistance of a device becomes greater than tens of kΩ, the transport is dominated by electron tunneling. In this regime most devices exhibit clean switching behavior with well defined P and AP states (Fig. 4.3, inset). Even after the metal bridge is broken, the size of the tunneling gap can still be adjusted by further electromigration. The shape of the MR curve and the values of the switching fields do not change significantly as electromigration changes the tunnel gap, but the value of the MR and even its sign can fluctuate over a wide range (Fig. 4.5). This suggests that the MR is sensitive to the details of the atomic structure near the tunnel gap. The tunneling current is flowing through just a few atoms on each of the electrodes, and the electronic structure at these atoms does not necessarily reflect the same degree of spin polarization as in the bulk of the ferromagnet [12]. The histogram of MR values we measure over 38 values of resistance in 20 tunneling devices is shown in the inset of Fig. 4.5. The MR values range from -10% to a maximum of 85%.

It is interesting to examine the bias voltage (V) dependence of the conductance and the MR. In the low resistance regime ($<$ 400 Ω), the MR is independent of V and the conductance decreases with bias (Fig. 4.6(a)), as it should because of increased backscattering at higher V in metallic devices. For high-resistance tunneling devices the conductance increases with V (Fig. 4.6(c)). In the intermediate regime (400 Ω to 25 kΩ), the conductance typically increases with V near V=0 as in the tunneling regime, but then decreases with V at higher biases as in the metallic regime. We interpret this as the effect of having both metallic channels

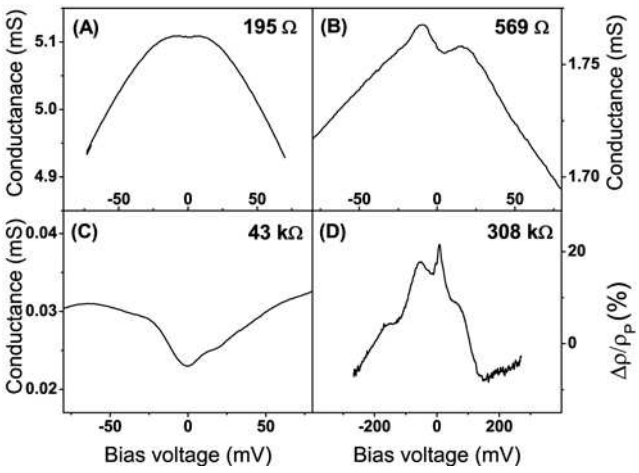


Figure 4.6: Differential conductance as a function of bias voltage for device IV at small (a), intermediate (b) and large (c) resistances. (d) Magnetoresistance as a function of bias for a tunneling device (device V).

and tunneling channels contributing in parallel. The MR in the tunneling regime displays strong dependence on V (Fig. 4.6(d)). The exact form of the dependence differs from device to device, but typically the MR drops by a factor of 2 on the scale of $V = 100$ mV. This is similar to the behavior of standard magnetic tunnel junctions with oxide barriers [11] and is in contrast to the STM experiments by Wulfhekel et al. [22], in which no voltage dependence of the MR was found for a vacuum tunneling gap.

In summary, using a combination of electron beam lithography and controlled electromigration, we fabricate ferromagnetic junctions with tunable cross section, with sizes ranging from 100×30 nm^2 to near the atomic scale. Further electromigration opens a tunneling gap between the electrodes. These devices do not have any suspended parts and are stable against magnetostriction and magnetostatic effects. We measure the magnetoresistance as a function of the cross-section of the constriction. When the cross-section is larger than approximately 1 nm^2 the MR

is less than 3% and increases as the cross-section decreases. For near-atomic-sized constrictions we observe MR as high as 80%, but find no devices in which the MR is as large as reported previously for the ballistic magnetoresistance mechanism [6, 7]. In the tunneling regime the MR values fluctuate over a wide range, -10% to 85%, even for small changes in the atomic structure near the constriction in a single device.

BIBLIOGRAPHY

[1] R. O'Handley, *Modern magnetic materials*, Wiley (2000).

[2] Kent A. D., Yu J., Rudiger U. and Parkin S. S. P., *J. Phys.: Condens. Matter* **13**, R461 (2001).

[3] Bruno P., *Phys. Rev. Lett.* **83**, 2425 (1999).

[4] Levy P. M. and Zhang S., *Phys. Rev. Lett.* **79**, 5110 (1997).

[5] Parkin S. S. P., *Annu. Rev. Mater. Sci.* **25** 357 (1995).

[6] Garcia N., Muoz M. and Zhao Y.-W., *Phys. Rev. Lett.* **82**, 2923 (1999).

[7] Hua S. Z. and Chopra H. D., *Phys. Rev. B* **67**, 060401 (2003).

[8] Gabureac M., Viret M., Ott F. and Fermon C., *Phys. Rev. B* **69**, 100401 (2004).

[9] H. D. Chopra, M. R. Sullivan, J. N. Armstrong, S. Z. Hua, *Nature Materials* **4**, 832 (2005).

[10] Egelhoff W. F. Jr., Gan L., Ettedgui H., Kadmon Y, Powell C. J., Chen P. J., Shapiro A. J., McMichael R. D., Mallet J. J., Moffat T. P., Stiles M. D., Svedberg E. B., *J. Magn. Magn. Mater.* **287**, 496 (2005).

[11] Tsymbal E. Y., Mryasov O. N., and LeClair P. R., *J. Phys.: Condens. Matter* **15**, R109 (2003).

[12] Jacob D., Fernndez-Rossier J., Palacios J. J., *Phys. Rev. B* **71**, 220403(R) (2005).

[13] Ozatay O., Chalsani P., Emley N. C., Krivorotov I. N. and Buhrman R. A., *J. Appl. Phys.* **95**, 7315 (2004).

[14] Montero M. I. *et al.*, *Phys. Rev. B* **70**, 184418 (2004).

[15] Pasupathy A. N. *et al.*, *Science* **306**, 86 (2004).

[16] OOMMF is Object Oriented MicroMagnetic Framework, a micromagnetic simulation code freely available from NIST at *http://math.nist.gov/oommf/* .

[17] Guillorn M. A. *et al.*, *J. Vac. Sci. Tech. B* **18**, 1177 (2000).

[18] Strachan D. R. *et al.*, *Appl. Phys. Lett.* **86**, 043109 (2005).

[19] Jansen A. G. M., van Gelder A. P., and Wyder P., *J. Phys C* **13**, 6073 (1980)

[20] Lepadatu S., Xu Y. B., *Phys. Rev. Lett.* **92**, 127201 (2004).

[21] Agrait N., Yeyati A. L., and van Ruitenbeek J. M., *Phys. Rep.* **377**, 81 (2003).

[22] Wulfhekel W., Ding H.F., Kirschner J., *J. Magn. Magn. Mater 242-245,* **47**, (2002).

[23] Z. K. Keane, L. H. Yu, and D. Natelson, *Appl. Phys. Lett.* **88** 062514 (2006).

[24] J. Velev and W. H. Butler, *Phys. Rev. B* **69**, 094425 (2005).

Chapter 5

Anisotropic magnetoresistance due to quantum interference in ferromagnets

5.1 Introduction

God runs electromagnetics by wave theory
on Monday, Wednesday, and Friday,
and the Devil runs them by quantum theory
on Tuesday, Thursday, and Saturday.
-Sir William Bragg

In the previous chapter we discussed the fabrication of ferromagnetic atomic-scale contacts and studied magnetic domain wall contribution to their resistance. We found that in a setup designed to neutralize magnetomechanical effects the entry of a domain wall into an atomic-size constriction *does not* lead to an extraordinary increase of magnetoresistance, in contrast with previous reports [5, 6] and we concluded that the reported magnetoresistances in excess of 1000% [6] likely resulted from magnetomechanical artifacts. Our observations, however, do not exclude the possibility of a smaller anomalous contribution due to electron scattering off an atomically-narrow domain wall [4].

To reexamine the possibility of such contribution we need to understand different mechanisms leading to a change in resistance in the presence of a domain wall. As discussed in the previous chapter, a domain wall may affect a ferromagnet's resistance through the conentional AMR effect. This is a purely macroscopic effect and it should be nulled out in order to observe the anomalous contribution due

to electron scattering. However, while well understood in the bulk, there is very little information of whether AMR changes for atomically-thin samples. Indeed, one recent experiment [11] hints that it may; an unusual increase of AMR is suspected in atomically-narrow nickel junctions. In addition, recent theory predicts dramatically changed AMR angle dependence to result from opening and closing of individual conductance channels in a ferromagnetic point contact [13].

These considerations motivate the experiments described in this chapter: We probe AMR as a function of the ferromagnetic contact's cross-section from 30 × 100 nm and into the near-atomic regime. To our surprise, we find that in atomic-sized contacts the AMR angular dependence deviates from its bulk form Eq. (1.10) and the size of the effect increases by almost two orders of magnitude. These results are interpreted as a consequence of conductance fluctuations due to mesoscopic interference. Before discussing the experiments, however, we briefly remind the reader the basics of mesoscopic conduction fluctuations for a simpler case of normal metals.

5.2 Brief overview: Mesoscopic conductance fluctuation due to quantum interference

In small samples at low temperatures quantum interference can significantly alter the classical Drude conductance. In disordered materials, the elastic scattering of the carriers from the impurities leads to random conductance fluctuation as a function of impurity configuration, magnetic field, and the position of the Fermi level. These fluctuations may be observed in micron-sized metallic or semiconducting wires or thin films; they arise because of the interference among the electron

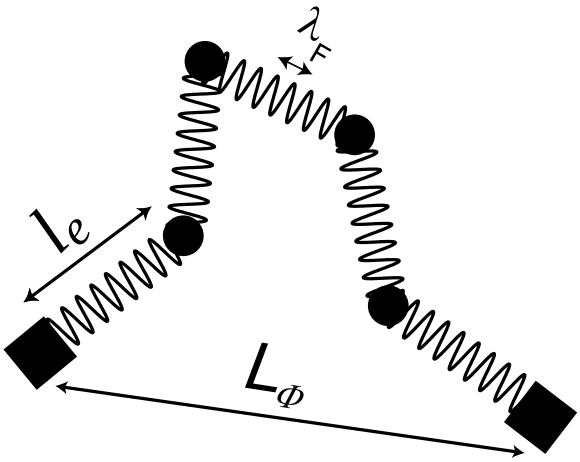


Figure 5.1: Cartoon diagram representing an electron's trajectory in diffusive metals when $\tau_e \ll \tau_\phi$. Circle represent elastic scattering from the impurities, squares represent inelastic scattering from phonons

waves scattered off different impurities [1].

The physics of mescopic conductance fluctuation is due to long-range coherence: elastic scattering of an electron from the impurities preserves the electron's phase. This condition may be written as $\tau_e \ll \tau_\phi$, where τ_e is the elastic scattering time and τ_ϕ is the phase coherence time, determined by inelastic scattering off phonons. Semiclassically, an electron's trajectory may be described by a three-dimensional diffusion, and the average distance L_ϕ electrons diffuses before losing coherence (called phase coherence length) may be evaluated as

$$L_\phi = \sqrt{D\tau_\phi}, \tag{5.1}$$

where $D = \frac{1}{3} v_F l_e$ is the diffusion constant and l_e is the elastic scattering length $v_F \tau_e$. Let's consider the interference between different electron trajectories for a system with all the dimensions smaller than L_ϕ, in the diffusive semiclassical limit

$$\lambda_F \ll l_e \ll L_\phi, \tag{5.2}$$

where λ_F is the Fermi wavelength $2\pi/k_F$ (Fig. 5.1). On the scale of L_ϕ the electron trajectory is coherent, and the system's conductance is determined by quantum interference among electron waves scattered from different impurities. Due to the randomness of impurities positions, the conductance oscillates randomly as a function of either the Fermi level position or magnetic field strength as quantified by the autocorrelation function $F(\Delta B, \Delta E) =< G(B+\Delta B, E+\Delta E), G(B,E) >$.

Measurement of the autocorrelation function provides an experimental way of extracting both coherence and elastic length scales. Under very general assumptions, both L_ϕ and l_e are easily obtained from the widths at half-maxium of $F(\Delta B, \Delta E)$ as a function of magnetic field ΔB_c and energy ΔE_c :

$$\Delta B_c = \frac{2e}{L_\phi^2} \tag{5.3}$$

$$\Delta E_c = \pi^2 \hbar v_F l_e / 3L_\phi^2. \tag{5.4}$$

Another important properties of the conductance fluctuation is that for different samples their size is universal

$$\Delta G \sim e^2/h \tag{5.5}$$

and independent of sample's background conduction or the nature of the disorder.

The formulas above are only valid for the case of small samples with all the dimensions $\sim L_\phi$ and low temperatures $kT < \pi^2 \hbar v_F l_e / 3L_\phi^2$. For smaller samples, the formulas (5.3),(5.4),(5.5) still hold with the coherence length L_ϕ replaced by the sample size L. For samples larger than L_ϕ the correlation scale ΔB_c and ΔE_c do not change, while the amplitude of the fluctuations decreases as a result of statistical averaging between many phase-coherent volumes L_ϕ^3.

Metallic point contacts provide a convenient platform to study conductance fluctuation in very small samples as a function of both electron energy (by ad-

justing the potential difference across the contact) and magnetic field [20, 19]. Different from the case of metallic wires discussed above, the size of the fluctuations in a point contact with the diamter a is reduced from the universal value $2e/h$ by approximately a/l_e. In addition, in point contacts with just a few quantum conductance channels contributing to the conductance the size of the fluctuation acquires a dependence on the transmission coefficient of the individual modes T_n [21].

5.3 Quantum interference in ferromagnets

The presence of ferromagnetism significantly complicates the physics of quantum interference. The problem is rather unexplored, only recently the first experimental [2, 30] and theoretical [3, 23] reports started to appear. There are several key factors altering the mechanism of quantum interference in ferromagnets compared to nornal metal [23]:

- Two spin channels with different densities of states $\nu_\downarrow$ and $\nu_\uparrow$ at the Fermi level contribute to the interference.
- Different densities of states result in different mean-free paths for the minority and the majority electrons.
- The spin channels may be "mixed" by the spin-orbit interaction without losing their coherence.

Adam *et al.* [23] considered the problem theoretically, introducing the following simplifying assumptions:

- The elastic scattering time is much shorter than the spin-orbit scattering time.

- The internal magnetic field in a feromagnet may be neglected in comparison with the exchange field.

- The calculation is done for an entirely spin-coherent sample of size L; care need to be taken to apply the results of the calculation to a device with $L_\phi < L$.

The calculation of Adam *et al.* predicts the appearance of conductance fluctuation due to quantum interference as a function of ferromagnet's *magnetization direction*, an easily observed and distinct signature. The experimental observation and interpretation of such fluctuations is the focus of the next section.

5.4 AMR due to quantum interference: the experiment

By making detailed studies of the resistance as a function of field angle using mechanically stable permalloy contacts, in this section we show that the size of the AMR signal at low temperatures can increase dramatically as the contact's cross section is narrowed to the nanometer-scale regime. Even more strikingly, we find that point contacts which are completely broken, so as to enter the tunneling regime, also exhibit a tunneling anisotropic magnetoresistance effect (TAMR) as large as 25% when the magnetic moments in the two contacts are rotated together while remaining parallel.

Magnetostriction and magnetostatic forces can alter the geometry of nanoscale junctions as the magnetic field is varied, and produce artifacts in the resistance, so experiments must be designed to minimize these effects [8, 9, 10]. For this reason, our contacts are firmly attached to a non-magnetic silicon substrate and are measured entirely at low temperature to suppress thermally-driven surface dif-

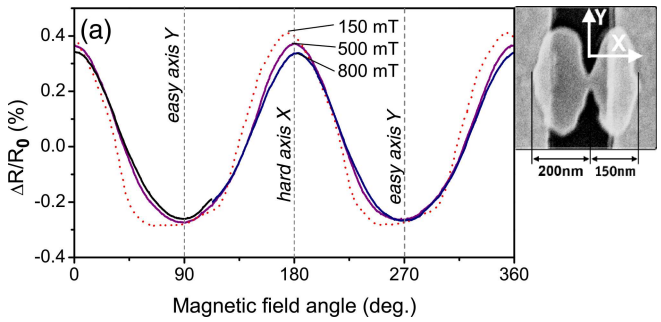


Figure 5.2: (a) Zero-bias differential resistance vs. angle of applied magnetic field at different field magnitudes at 4.2 K, illustrating bulk AMR for a constriction size of 30×100 nm^2 and resistance $R_0 = 70\ \Omega$ (device A). (b) SEM micrograph of a typical device.

fusion of metal atoms. Similar structures have proven [11, 12] to be much more mechanically-stable than previous samples which were measured at room temperature. We fabricate our devices using aligned steps of electron beam lithography to first pattern 20-nm-thick gold contact pads and then 30-nm-thick magnetic permalloy (Py = $Ni_{80}Fe_{20}$) point contacts [12]. Each contact consists of two elongated electrodes which are connected by a 100-nm-wide bridge (Fig. 5.2(b)). The magnetic field $\mathbf{B}$ is applied using a 3-coil vector magnet capable of 0.9 T in any direction and up to 7 T along one axis (the x axis, defined below) with the other two coils turned off. The differential resistance $R = dV/dI$ at voltage bias V is measured using a lock-in amplifier with an excitation voltage small enough not to broaden the data; a total of 46 devices were studied.

Measurements are performed as follows: we first cool the samples to 4.2 K and narrow the size of the bridge connecting the two magnetic electrodes by using actively controlled electromigration [14]. When the desired cross-section is reached (as determined by the sample's R) we stop the electromigration process and mea-

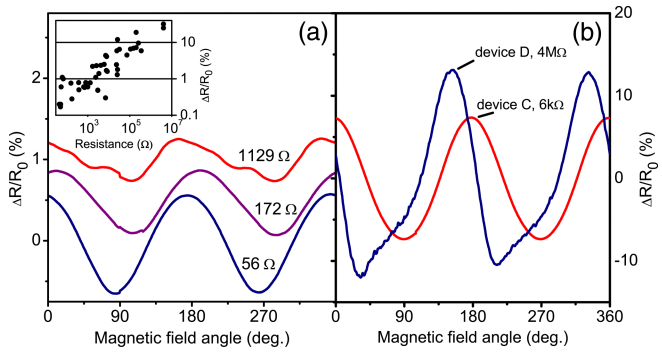


Figure 5.3: (a) Evolution of AMR in device B as its resistance R_0 is increased from 56 Ω to 1129 Ω. (b) AMR for a $R_0 = 6$ kΩ device (device C) exhibiting 15% AMR, and a $R_0 = 4$ MΩ tunneling device (device D), exhibiting 25% TAMR. All measurements were made at a field magnitude of 800 mT at 4.2 K. Inset: AMR magnitude as a function of R_0 for 12 devices studied into the tunneling regime.

sure R at 4.2 K while rotating the magnetic field in the plane of the sample at fixed magnitude. Then the same procedure is repeated to achieve smaller device cross-sections and larger R. As a result we can examine magnetic properties of each device as a function of the bridge size, down to the atomic scale and into the tunneling regime [12].

The resistances of all devices before electromigration (≈ 70 Ω at 4.2 K) exhibit a small periodic dependence on the field direction ($\sim 1\%$, Fig. 5.2(a)). This is a signature of the bulk anisotropic magnetoresistance (AMR), which for a polycrystalline sample may be written as $\Delta R \propto \cos^2(\theta)$, where θ is the angle between the current and the magnetization $\mathbf{M}$ [15]. The resistance of our devices before electromigration is maximal for $\mathbf{B}$ applied in the x-direction (Fig. 5.2(b)), parallel to the current. We measure θ relative to this direction.

Because the AMR depends on the orientation of the magnetization, it is important to ensure that the sample is magnetized uniformly and always remains

saturated in the direction of the applied field. We estimated the distribution of magnetization within our sample using the OOMMF code [16]. Such modeling suggests that applying 800 mT effectively saturates the nanoscale magnetic electrodes for all directions in plane: the average $\mathbf{M}$ follows $\mathbf{B}$ to within 2° and the RMS fluctuation in the angle of magnetization across the sample is $\sigma_{\mathbf{M}} < 4°$. To check this experimentally, we fit our 800 mT data to $\Delta R \propto \cos^2(\theta)$, and we found that the RMS deviation of the magnetization angle indicated by the fit was $\sigma_{\mathbf{M}} < 5°$. We observe that the applied field becomes insufficient to fully saturate $\mathbf{M}$ below approximately 200 mT, at which point $\mathbf{M}$ departs from the field direction toward the easy axis of the sample (Fig. 5.2(a), dotted curve). We performed similar studies also for samples in the tunneling regime and for near-atomic-sized contacts. In addition, we performed sweeps to 7 Tesla along the hard in-plane axis (x axis) for one sample having $R = 3$ kΩ in the metallic range and two samples in the tunneling regime 200, 400 kΩ. (Device E with $R = 2.6$ kΩ was measured to 3.5 T.) In all cases we found that 0.8 T in-plane magnetic fields were sufficient to saturate the resistance.

As the cross section of the device is narrowed for samples with $R < 500$ Ω, both the phase and the amplitude of the AMR can change, but the AMR remains small and retains its $\cos^2(\theta)$ dependence (Fig. 5.3(a), $R = 172$ Ω). The changes in phase and amplitude may be a result of changes in sample geometry during electromigration. Scanning electron microscopy studies show changes large enough to alter the direction of current flow in the junction.

As the cross-section is reduced further, to the regime where R is larger than several hundred Ω, the angular dependence of the AMR for some samples (Fig. 5.3(a)) can become more complicated than the simple $\cos^2(\theta)$ form. In addition, we find

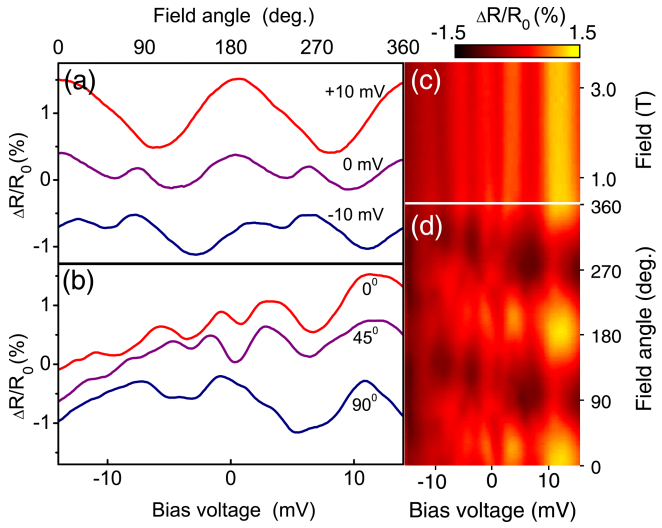


Figure 5.4: Variations of $R = dV/dI$ at 4.2 K in a sample with average zero-bias $R_0 = 2.6$ kΩ (device E). (a) R vs. field angle at different bias voltages ($|B| = 800$ mT). (b) Dependence of R on V at different fixed angles of magnetic field ($|B| = 800$ mT). The curves in (a) and (b) are offset vertically. (c) R as a function of V and magnetic field strength, with field directed along the x axis. R does not have significant dependence on the magnitude of B. (d) R as a function of V and θ, for $|B| = 800$ mT.

that devices with R larger than $\sim$1 kΩ generally exhibit larger AMR. Figure 5.3(b) shows a 6 kΩ device with an AMR of 14% (device C), more than 50 times the value for this device before electromigration. Even for samples in the tunneling regime ($R > h/e^2 \approx 26$ kΩ) we continue to measure large values of AMR, as large as 25% in a 2 MΩ sample (Fig. 5.3(b), device D). The dependence of the AMR on sample resistance is shown in Fig. 5.3, Inset.

We can gain insight into the mechanism behind the large AMR and TAMR effects from their dependence on bias voltage. There are significant changes in the angular dependences of dV/dI for voltages differing by just a few mV (Figs. 5.4(a), 5.5(a)). Moreover, at fixed field angle, dV/dI also exhibits reproducible fluctuations as a function of V (Figs. 5.4(b),5.5(b)). These fluctuations depend only on the angle of the applied field, not on its strength (Figs. 5.4(c),5.5(c)). For both the metallic and tunneling samples the size of the AMR effect is similar to the magnitude of fluctuations in dV/dI as a function of V.

Before discussing other mechanisms, we consider the possibility of artifacts due to magnetostriction and magnetostatic forces. Neither of these effects should produce smooth fluctuations in R as a function of small changes in V. Furthermore, for samples with R near that of a single quantum channel, these effects are known to cause atomic rearrangements manifested as irreproducible jumps in R [8], a feature not seen in any of our data. We can estimate the consequences of magnetostriction in the tunneling regime by assuming that the magnetostriction constant in Py is $\lambda_s < 10$ ppm and the length of any suspended region in our device is < 10 nm, so that any displacement is < 10 fm. Applying the Simmons formula for tunneling [17] with a work function < 5 eV, the change in R due to this displacement would be $< 0.4\%$, more than 50 times smaller than the AMR we observe for tunneling

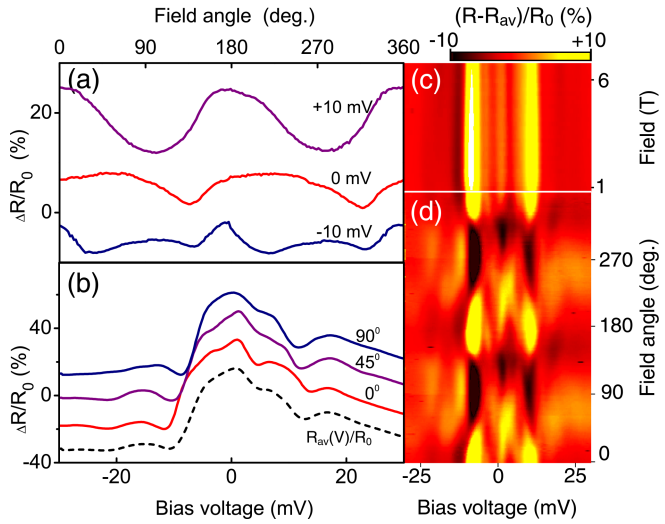


Figure 5.5: Variations of $R = dV/dI$ at 4.2 K in a sample with average zero-bias $R_0 = 257$ kΩ (device F), in the tunneling regime. (a) R vs. field angle at different bias voltages ($|B| = 800$ mT). (b) Dependence of R on V at different fixed angles of magnetic field ($|B| = 800$ mT). The curves in (a) and (b) are offset vertically. (c) $R(V) - R_{\rm av}(V)$ as a function of V and magnetic field strength, with field directed along the x axis. $R_{\rm av}(V)$, the average of $R(V)$ over angle (shown in (b)), is subtracted to isolate angular-dependent variations. (d) $R(V) - R_{\rm av}(V)$ as a function of bias voltage and magnetic field angle, for $|B| = 800$ mT.

devices. Magnetostatic forces would give changes in R of the opposite sign than we measure for many samples. We conclude that neither magnetostriction nor magnetostatic effects can account for our enhanced AMR signals.

Fluctuations in R as a function of V, similar to those we measure, have been observed previously in non-magnetic samples and are understood to be a signature of mesoscopic quantum interference of scattered electron waves [18]. For diffusive metal samples with a characteristic size similar to the dephasing length, the magnitude of the fluctuations has a universal scale when expressed in terms of the conductance ($G = dI/dV = 1/R$): $\Delta G \sim e^2/h$ in nonmagnetic samples with weak spin-orbit scattering and $\Delta G \sim 0.4\ e^2/h$ in magnetic samples with spin-orbit scattering [18]. However, the conductance fluctuations in non-magnetic point-contact devices with a contact radius less than the elastic mean free path l_e have smaller, non-universal magnitudes [19, 20, 21]. The average magnitude of the fluctuations that we measure in samples with R = 1-14 kΩ is 0.1 e^2/h. Conductance fluctuations as a function of V have also been observed previously for small non-magnetic tunnel junctions [22], and are understood to be a consequence of mesoscopic fluctuations in the local density of electronic states of a disordered sample. Because the variations that we measure in R as a function of θ have a magnitude similar to the fluctuations as a function of V, we propose that the dominant process giving rise to enhanced AMR and TAMR in our samples is mesoscopic interference, as well.

Unlike previous measurements in non-magnetic devices [19, 22], we do not observe fluctuations as a function of the magnitude of magnetic field up to at least 7 T (Figs. 5.4(c),5.5(c)), only as a function of θ. Based on the data, we estimate that the correlation scale for fluctuations as a function of field magnitude

must be $B_c > 20$ T. We therefore conclude that our AMR and TAMR cannot be due directly to the magnetic field affecting the Aharonov-Bohm phase of the electrons; the maximum change in total field through the sample upon rotating the magnetization by 90° at 0.8 T is only $\sqrt{2}(\mu_0 M_s + 0.8\text{ T}) \sim 2.7$ T, where $\mu_0 M_s = 1.1$ T is the magnetization for permalloy. However, an alternative mechanism was recently proposed by Adam *et al.* [23], that rotation of the magnetization direction in ferromagnets may alter quantum interference because it is coupled to the electrons' orbital motion via spin-orbit scattering. As a result, mesoscopic fluctuations in the conductance of magnetic metal samples and in the local density of states of magnetic tunneling devices can be expected to occur as a function of the magnetization orientation.

The theory of Adam *et al.* [23] was solved for the case of diffusive samples, and therefore one should not expect it to be quantitative for our point contacts. Nevertheless, we will compare the results of this theory to our measured correlation scales, to test whether the mechanism of Adam *et al.* might provide a reasonable qualitative explanation. The voltage correlation scale for our data is $V_c \approx$ 1-2 mV, approximately equal to the limit set by thermal broadening at 4.2 K. The zero-temperature energy correlation scale E_c can be calculated by the formalism in ref. [23] to be

$$E_c = (E_T^{\uparrow}\tau_{\perp}^{\uparrow} + E_T^{\downarrow}\tau_{\perp}^{\downarrow})/(\tau_{\perp}^{\downarrow} + \tau_{\perp}^{\uparrow}), \tag{5.6}$$

where $E_T^{\uparrow}$ and $E_T^{\downarrow}$ are the Thouless energies for spin-up and spin-down s,p-band electrons and $\tau_{\perp}^{\uparrow}$ and $\tau_{\perp}^{\downarrow}$ are spin-flip spin-orbit scattering times [24]. In permalloy, because of the contribution of the minority-electron d-band, the density of states at the Fermi level for minority electrons $\nu^{\downarrow}$ is much greater than for majority electrons, so by Fermi's golden rule we can estimate $\tau_{\perp}^{\downarrow} \propto (\nu^{\uparrow})^{-1} \gg \tau_{\perp}^{\uparrow} \propto (\nu^{\downarrow})^{-1}$ and $E_T^{\uparrow}\tau_{\perp}^{\uparrow} \approx$

$E_T^{\downarrow}\tau_{\perp}^{\downarrow} \propto (\nu^{\uparrow}\nu^{\downarrow})^{-1}$. Eq. (5.6) then takes a simple form, $E_c \sim 2E_T^{\downarrow} \sim 2\pi^2\hbar v_F l_e^{\downarrow}/3L_\phi^2$, where $v_F = 0.2\times10^6$ m/s is the Fermi velocity in Py [25], $l_e^{\downarrow} \sim 0.6$ nm is the elastic mean free path for minority electrons [25, 26], and L_ϕ is the dephasing length. Assuming that the voltage correlation scale $V_c \sim \max\{k_BT/e, E_c/e\}$, we find a rough lower limit on the dephasing length, $L_\phi > 16$ nm. If L_ϕ is close to this value, then the magnetic field correlation scale $B_c \sim \Phi_0/L_\phi^2 \sim 16$ T, in reasonable agreement with our estimate from the field dependence. The formalism in ref. [23] can also be used to predict the correlation angle for the fluctuations [24]:

$$\theta_c \sim \sqrt{\frac{2}{\hbar}\left(E_T^{\uparrow}\tau_{\perp}^{\uparrow} + E_T^{\downarrow}\tau_{\perp}^{\downarrow}\right) \Big/ \left(2 + \frac{\tau_{\perp}^{\uparrow}}{\tau_{\parallel}^{\uparrow}} + \frac{\tau_{\perp}^{\downarrow}}{\tau_{\parallel}^{\downarrow}}\right)}, \tag{5.7}$$

where $\tau_{\parallel}^{\uparrow}$ and $\tau_{\parallel}^{\downarrow}$ are mean free times for spin-conserving spin-orbit scattering. Employing golden-rule assumptions similar to those we used above: $\tau_{\perp}^{\uparrow}, \tau_{\parallel}^{\downarrow} \propto (\nu^{\downarrow})^{-1}$ and $\tau_{\perp}^{\downarrow}, \tau_{\parallel}^{\uparrow} \propto (\nu^{\uparrow})^{-1}$, we find $\theta_c \sim 2(\tau_{\parallel}^{\downarrow}E_T^{\downarrow}/\hbar)^{1/2} \sim \frac{2\pi}{\sqrt{3}}(\tau_{\parallel}^{\downarrow}/\tau_e^{\downarrow})^{1/2} l_e^{\downarrow}/L_\phi$. With the approximations $\tau_{\parallel}^{\downarrow} \sim 2\tau_{\perp}^{\uparrow}$ [24], $\tau_{\perp}^{\uparrow} \sim (5.5\text{nm})/v_F$ [27], our estimate for θ_c is ~ 0.6 radians. Considering the rough nature of the approximations, we consider this to be in good agreement with our measurements – typically we see one or two oscillations in dV/dI as a function of θ over the relevant range of 0 to π radians. (By inversion symmetry, R at V=0 must be unchanged upon rotation by π.)

Large TAMR signals, qualitatively similar to our results in the tunneling regime, were also reported recently in (Ga,Mn)As magnetic semiconductor tunnel junctions [28]. However, the mechanism proposed to explain the (Ga,Mn)As measurements is a band-structure effect by which the *bulk* density of states depends on magnetization angle [28, 29]. This is fundamentally distinct from our proposal that TAMR effects in nanoscale metal devices are due to mesoscopic fluctuations in the *local* density of states. As already noted in ref. [23], mesoscopic fluctuations

as a function of magnetization angle may be relevant in describing another recent experiment [30], which was originally analyzed in terms of the motion of magnetic domain walls.

In summary, we have measured the AMR of ferromagnetic metal contacts at low temperature as a function of their size, over the range from large (100×30 nm^2) cross sections to atomic-scale point contacts and into the tunneling regime. For metallic devices with R larger than ~ 1 kΩ we observe AMR effects larger than in bulk devices, with an angular variation that can deviate from the sinusoidal bulk dependence, and which are associated with fluctuations in R of similar magnitude as a function of V. Similar effects are also seen in magnetic point-contact tunneling devices. We propose that these large AMR and TAMR effects are the result of mesoscopic quantum interference which depends on the orientation of the magnetization, leading to fluctuations of conductance and the spin-dependent local density of states. These fluctuations should affect a broad variety of nanoscale devices that contain magnetic components, producing strong perturbations in measurements of low-temperature spin-dependent transport.

5.5 Looking back: domain walls & quantum inteference

In Chapter 4 we explored the possibility of the anomalous electron scattering from the atomically-narrow domain wall. There, we changed *the strength* of the magnetic field along the x axis of the ferromagnet (Fig. 4.2) so as to create a domain wall at around zero field; the resulting change in resistance at $H = 0$ allowed setting the upper bound on the strength of this scattering. As discussed earlier, a domain wall can contribute to ferromagnet's resistance in several different ways:

1. Anisotropic manetoresistance may contribute to the resistance of the domain

wall because of the magnetization direction change at the location of the wall.

2. When the width of the domain wall is comparable to the Fermi wavelength, electrons cannot adiabatically follow the magnetization profile, resulting in anomalous backscattering and a large increase in resistance [4, 32].

3. The presence of a domain wall inside a tunneling gap in a ferromagnetic wire causes tunneling magnetoresistance contribution (see Introduction).

In the previous chapter we silently assumed that the size of the AMR is always small, and ascribed any change in resistance in excess of several percent in metallic wires at around zero field to the second mechanism. We have now seen that this assumption is not valid: anisotropic magnetoresistance may be enhanced dramatically in nanoscale conductors and contribute to the resistance of the wall. Hence, it now seems appropriate to re-analyze the data of Chapter 4 in light of this new knowledge in order to separate the "geometrical" AMR contribution from the anomalous backscattering. It is also interesting to examine the influence of the domain wall on the pattern of quantum interference: it was predicted, for example, that the presence of the wall may result in a topological Berry phase [33, 34].

We can gain some insight into the mechanism of the domain wall contribution by comparing the dependence of the ferromagnet's resistance on two different variables:*the angle* of the applied magnetic field and the *field strength* at constant field angle. To understand how the contributions are separated, we examine the magnetoreistance of a 60 Ω device. (device F, Fig. 5.6). We note two things: First, the full resistance change as a function of field strength (Fig. 5.6(b)) is smaller than the resistance change as a function of field direction (Fig. 5.6(a)). Second, the resistance at zero field in Figure 5.6(b) is either at a maximum or at a minimum

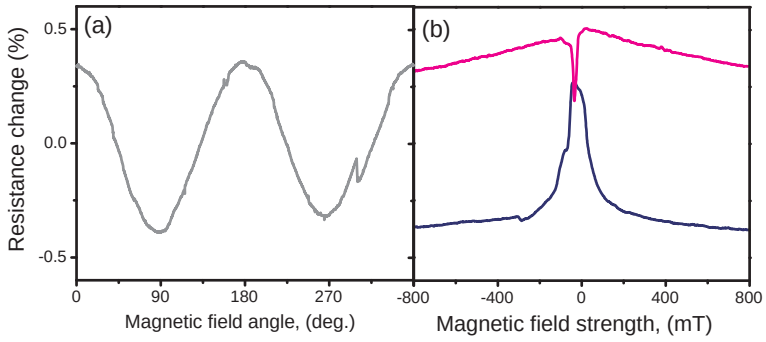


Figure 5.6: Domain wall contribution to the magnetoresistance for a 60 Ω permalloy device. (a) Change in resistance as a function of magnetic field angle. (b) Change in resistance as a function of magnetic field strength; the field is applied along the x axis (blue curve) and y axis (pink curve)

depending on the direction of the applied field. These observations are fully consistent with the domain wall contribution fully coming from the AMR effect: The magnetization *only* changes its direction at the wall location and the contribution due to the wall is smaller than the full size of the AMR; When the field applied parallel to the current the AMR resistance change due to the presence of the wall is negative, and positive otherwise. In our measurements, this behavior is typical in devices large compared to the atomic scale, and to no surprise we conclude that the resistance of a "wide" domain wall is fully explained by the AMR contribution.

The situation changes for higher-resistance devices, such as a 19 kΩ device. (device G, Fig. 5.7). The resistance change due to the domain wall is now positive regardless of field direction; the change is larger than the full size of the AMR contribution (Fig. 5.7(a)). We can thus argue that the resistance change at around zero field is at least in part coming from a mechanism different from anisotropic magnetoresistance. In order to ascribe the resistance change to either TMR or

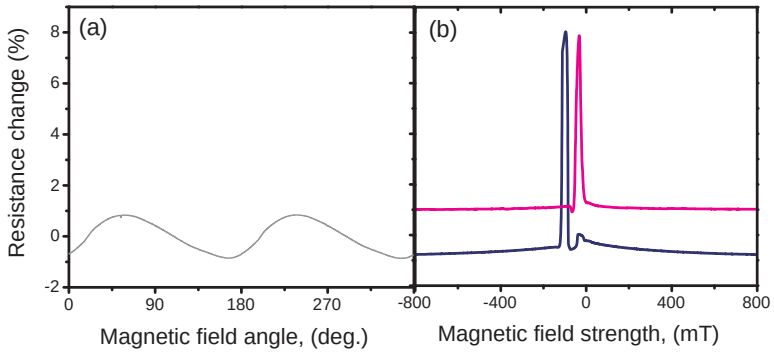


Figure 5.7: Domain wall contribution to magnetoresistance for a 7 kΩ permalloy device. (a) Change in resistance as a function of magnetic field angle. (b) Change in resistance as a function of magnetic field strength; the field is applied along the x axis (blue curve) and y axis (pink curve)

anomalous scattering we need to determine whether the conductance of the device is predominantly metallic or tunneling. Although in principle measuring the conductance as a function of bias voltage should allow such discrimination (the conductance increases with bias in the tunneling regime and decreases in metallic regime), fast oscillations of conductance as a function of voltage make discrimination between metallic and tunneling devices impossible (Fig. 4.6).

In summary, comparing the dependence of conductance on field angle and field strength allows us to draw the following conclusions:

- For low-resistance devices $R \leq 500\ \Omega$ the domain wall resistance is fully accounted for by the AMR effect.

- There is a contribution to the domain wall resistance in the intermediate regime of atomic-sized point contacts $500\ \Omega \leq R \leq 25\ k\Omega$ which is not explained by AMR. This contribution is either due to tunneling magnetoresistance or anomalous scattering of electrons by a sharp potential of the

domain wall.

- Surprisingly, in the tunneling regime $R \geq 25\ k\Omega$ both the enhanced AMR and tunneling magnetoresistance contribute to the resistance of a domain wall. This observation can explain the data of Keane *et al.* [11].

It is also interesting to examine the influence of the domain wall on the pattern of quantum interference [33, 34]. The problem was experimentally studied by Wei *et al.* [30] who claimed to observe a shift in interference due to electrons "mistracking" the magnetization of the domain wall. Whereas the shift in interference pattern is also seen in our data (note abrupt changes in interference around $H = -25\ mT$ and $H = +5\ mT$ in Fig. 5.8(b)), our results cast some doubt on the explanation of Wei *et al.* Comparing Figs. 5.8(a) and 5.8(b) we see that at least in part the change in interference at around zero field is caused by the "geometrical" contribution due to AMR. We are presently trying to understand whether there are some features not accounted for by this geometrical contribution.

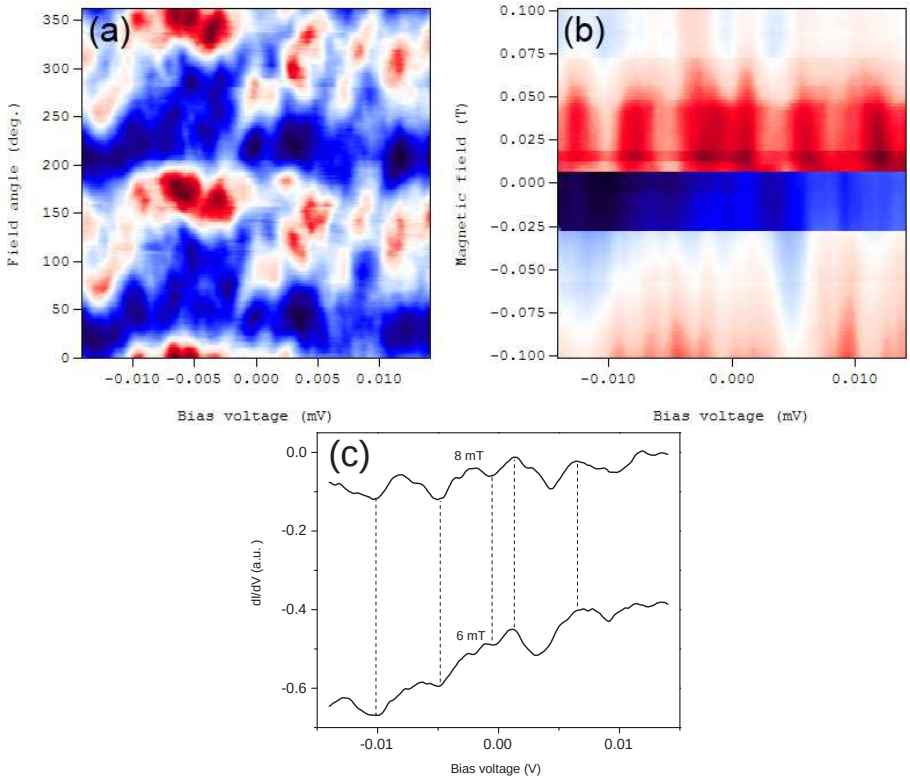


Figure 5.8: Domain wall contribution to mesoscopic interference for 19 kΩ permalloy device. (a) R(V) as a function of bias voltage and magnetic field angle, for $\|B\| = 800$ mT (b) R(V) as a function of magnetic field strength, with magnetic field directed along the x axis. Note the switching events near zero field. (c) R(V) as a function of bias voltage for $\|B\| = 6$ mT and $\|B\| = 8$ mT. Note the change in resistance.

BIBLIOGRAPHY

[1] S. Washburn and R. A. Webb, *Rep. Prog. Phys.* **55**, 1311 1992.

[2] S. Lee, A. Trionfi, and D. Natelson, *Phys. Rev. B* **70**, 212407 (2004).

[3] V. K. Dugaev, P. Bruno, and J. Barnas, *Phys. Rev. B* **64**, 144423 (2001).

[4] P. M. Levy and S. F. Zhang, Phys. Rev. Lett. **79**, 5110 (1997).

[5] N. Garcia, M. Munoz, and Y. W. Zhao, Phys. Rev. Lett. **82**, 2923 (1999).

[6] S. Z. Hua and H. D. Chopra, Phys. Rev. B **67**, 060401(R) (2003).

[7] M. Viret, S. Berger, M. Gabureac, F. Ott, D. Olligs, I. Petej, J. F. Gregg, C. Fermon, G. Francinet, and G. Le Goff, Phys. Rev. B **66**, 220401(R) (2002).

[8] M. Gabureac, M. Viret, F. Ott, and C. Fermon, Phys. Rev. B **69**, 100401(R) (2004).

[9] C. S. Yang, C. Zhang, J. Redepenning, and B. Doudin, Appl. Phys. Lett. **84**, 2865 (2004).

[10] W. F. Egelhoff, L. Gan, H. Ettedgui, Y. Kadmon, C. J. Powell, P. J. Chen, A. J. Shapiro, R. D. McMichael, J. J. Mallett, T. P. Moffat, J. Magn. Magn. Mater. **287**, 496 (2005).

[11] Z. K. Keane, L. H. Yu, and D. Natelson, *Appl. Phys. Lett.* **88** 062514 (2006).

[12] K. I. Bolotin, F. Kuemmeth, A. N. Pasupathy, and D. C. Ralph, Nano Lett. **6**, 123 (2006).

[13] J. Velev, R. F. Sabirianov, S. S. Jaswal, and E. Y. Tsymbal, Phys. Rev. Lett. **94**, 127203 (2005).

[14] D. R. Strachan, D. E. Smith, D. E. Johnston, T. H. Park, M. J. Therien, D. A. Bonnell, and A. T. Johnson, Appl. Phys. Lett. **86**, 043109 (2005).

[15] T. R. Mcguire and R. I. Potter, IEEE Trans. on Magn. **11**, 1018 (1975).

[16] OOMMF is Object Oriented MicroMagnetic Framework, a simulation code available from NIST at http://math.nist.gov/oommf/.

[17] E. L. Wolf, *Principles of Electron Tunneling Spectroscopy* (Oxford Univeristy Press, New York, 1989).

[18] P. A. Lee, A. D. Stone, and H. Fukuyama, *Phys. Rev. B* **35**, 1039 (1987).

[19] P. A. M. Holweg, J. A. Kokkedee, J. Caro, A. H. Verbruggen, S. Radelaar, A G. M. Jansen, and P. Wyder, *Phys. Rev. Lett.* **67**, 2549 (1991).

[20] D. C. Ralph, K. S. Ralls, and R. A. Buhrman, *Phys. Rev. Lett.* **70**, 986 (1993).

[21] B. Ludoph, M. H. Devoret, D. Esteve, C. Urbina, and J. M. van Ruitenbeek, *Phys. Rev. Lett.* **82**, 1530 (1999).

[22] A. van Oudenaarden, M. H. Devoret, E. H. Visscher, Yu. V. Nazarov, and J. E. Mooij, *Phys. Rev. Lett.* **78**, 3539 (1997).

[23] S. Adam, M. Kindermann, S. Rahav, and P. W. Brouwer, *Phys. Rev. B* **73**, 212408 (2006)

[24] S. Rahav and P. W. Brouwer, unpublished.

[25] D. Y. Petrovykh, K. N. Altmann, H. Höchst, M. Laubscher, S. Maat, G. J. Mankey, and F. J. Himpsel, *Appl. Phys. Lett.* **73**, 3459 (1998).

[26] B. A. Gurney, V. S. Speriosu, J.-P. Nozieres, H. Lefakis, D. R. Wilhoit, and O. U. Need, *Phys. Rev. Lett.* **71**, 4023 (1993).

[27] S. D. Steenwyk, S. Y. Hsu, R. Loloee, J. Bass, and W. P. Pratt Jr., *J. Magn. Magn. Mater.* **170**, L1 (1997).

[28] C. Gould, C. Ruster, T. Jungwirth, E. Girgis, G. M. Schott, R. Giraud, K. Brunner, G. Schmidt, and L. W. Molenkamp, *Phys. Rev. Lett.* **93**, 117203 (2004).

[29] A. B. Shick, F. Maca, J. Masek, and T. Jungwirth, *Phys. Rev. B* **73**, 024418 (2006).

[30] Y. G. Wei, X.Y. Liu, L.Y. Zhang, and D. Davidović, *Phys. Rev. Lett.* **96**, 146803 (2006).

[31] M. Viret, M. Gabureac, F. Ott, C. Fermon, C. Barreteau, and R. Guirado-Lopez, *cond-mat/0602298*.

[32] J. Velev and W. H. Butler, *Phys. Rev. B* **69**, 094425 (2005).

[33] Y. Lyanda-Geller, I. L. Aleiner, and P. M. Goldbart, *Phys. Rev. Lett.* **81**, 3215 (1998).

[34] G. Tatara, H. Fukuyama, *Phys. Rev. Lett.* **78**, 3773 (1997).

Chapter 6

Conclusions and possible experiments

If Murphy's Law can go wrong, it will

- Silverman's Paradox

In the past chapters we have seen how the initial goal of exploring single spins in SETs led us to explore a variety of fascinating physics in what one might think should be simple systems. We have discussed how efficient gating in an SET can be implemented by using a lateral fabrication geometry and have seen that in gold nanoparticles electrons fill particle-in-a-box states as in a non-interacting model. We examined the use of chemical self-assembly to fabricate an SET's island and found that it results in stable and predictable devices with well resolved electronic states. We have used controlled electromigration to study atomic-sized magnetic electrodes and found a surprising increase in AMR which we interpreted as a consequence of mesoscopic interference. We have also examined the contribution of domain walls to ferromagnets magnetoresistance and found no credible evidence for the controversial "ballistic magnetoresistance".

Not to anyone's surprise, the yellow brick road of experiments turned out even windier than expected. The journey has started with the initial goal of studying ferromagnetic SETs and now, some four years later, we are trying to understand domain walls contribution to mesoscopic conductance fluctuation in ferromagnets. However, we have made a considerable advancement towards our initial goal and in this last chapter we (somewhat nostalgically) review our progress in controllable spin injection into an SET and outline the problems we encountered. In addition, we discuss several promising experiments we have tried but did not have time to

finish and several promising ideas we have considered but did not have time to shape into experiments.

6.1 Progress towards ferromagnetic SETs

The entire infrastructure is now at hand to study SETs with ferromagnetic electrodes: an efficient gate electrode, controllable island and tunnel barriers, and well-characterized magnetic electrodes. We were able to put these components together: we fabricated devices with ferromagnetic (nickel) electrodes, e-beam evaporated gold nanoparticle island (following the fabrication recipe from Chapter 2) and aluminum oxide gate electrode; the devices were capped with 30 nm of e-beam evaporated aluminum oxide to ensure mechanical stability and in an attempt to prevent oxidation of the electrodes. Conductance (colorscale) as a a function of both gate and bias voltage for one such device is shown in Fig. 6.1

The device exhibits SET behavior at low temperatures and a spectrum of quantum-particle-in-a-box states is clearly resolved. We looked for the signatures of spin transport by examining the evolution of electron states as a function of magnetic field (applied in the device plane), as magnetization of the electrodes is switched from a parallel (P) to antiparallel (AP) state. As we see, the relative intensities of the conductance peaks change as magnetization is first switched from P to AP at around $H = +30$ mT and then are restored as the magnetization is switched back to P state at around $H = +90$ mT (Fig. 6.2). As discussed in the introductory chapter, this may be interpreted as a signature of spin-accumulation on the SET island.

However, the device cannot be described by a simple model of a normal-metal island coupled to ferromagnetic leads: the conductance as a function of field is

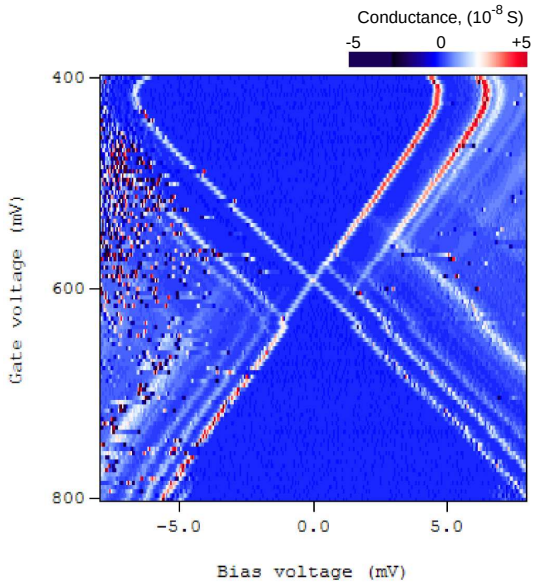


Figure 6.1: Conductance (colorscale) as a function of gate and bias voltage for an SET with gold island and nickel electrodes.

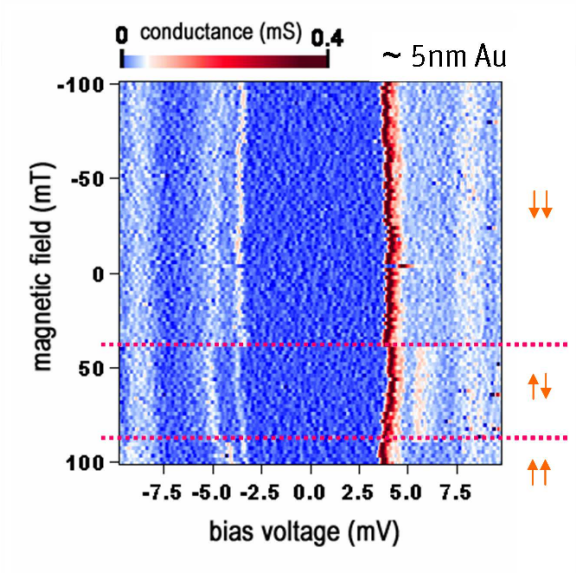


Figure 6.2: Conductance (colorscale) as a function of magnetic field and bias voltage for a metallic SET with gold island and ferromagnetic (nickel) leads. Note the shift of particle-in-a-box states around +40 mT

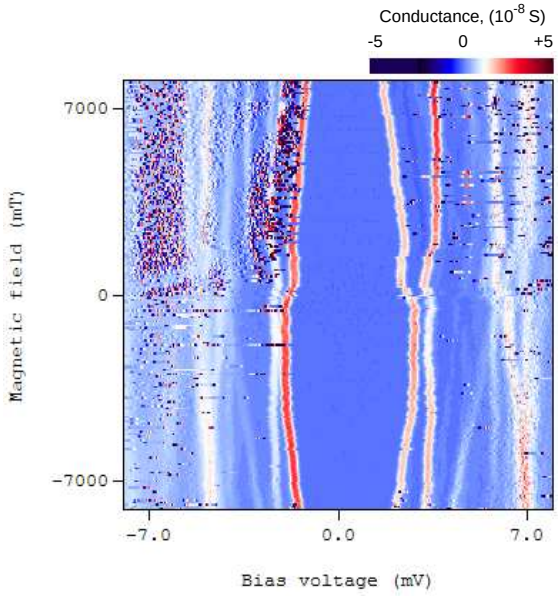


Figure 6.3: Conductance (colorscale) as a function of the applied magnetic field from -8 T to +8 T and bias voltage for an SET with gold island and nickel electrodes. Note the asymmetry in the electron levels with respect to zero field.

not symmetric with respect to zero (Fig. 6.3). This hints that the experiment is affected by an artifact producing an uncompensated magnetic field affecting the device. Such artifacts are commonly seen in oxidized ferromagnets and we may speculate that antiferromagentic oxide is formed on the surface of the electrodes in the ambient atmosphere. This may result in exchange biasing and associated uncompensated exchange field; this exchange field may in turn unpredictably affect the magnetic behavior of the device.

We need to review the fabrication process to understand how this problem may come about: during the fabrication, we load the devices into the evaporator and pump it down to better than 2×10^{-7} vacuum. We then perform electromigration to create ferromagnetic electrodes, evaporate a submonolyer of gold to create nanoparticles, and finally deposit a capping layer of aluminum oxide. We know that electromigration results in oxide-free tunnel junctions: the experiments of Chapters 4 and 5 do not show any signs of exchange biasing in ferromagnetic devices formed in cryogenic vacuum. Thus, we may speculate that the aluminum oxide capping layer does not offer ferromagnetic electrodes enough protection against oxidation in ambient atmosphere; the electrodes are oxidized as soon as the evaporator's chamber is opened to air.

We designed a simple experiment to check this hypothesis. In this experiment, the resistance of a ferromagnetic tunneling gap is monitored from the moment of electromigration to the moment when the evaporator chamber is opened to air. Figure 6.4 clearly demonstrates an abrupt drop in the tunneling gap's resistance precisely when the chamber is opened to air, confirming the proposed mechanism of electrode oxidation. We have tried different combinations of capping layer materials: aluminum oxide, silicone oxide, silicone dioxide, silicone nitride. Unfor-

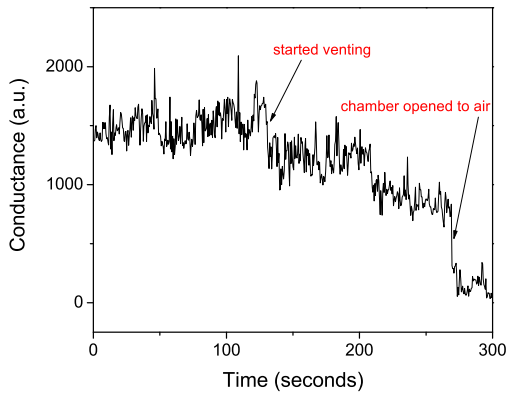


Figure 6.4: The conductance of a ferromagnetic tunneling gap protected by aluminum and silicone oxide capping layers monitored after electromigration. The conductance slowly decreases as the chamber is vented with dry nitrogen and drops to zero as the chamber is opened to air, suggesting that ferromagnetic electrodes may be oxidized.

tunately, none of these materials prevent oxidation of the electrodes as confirmed by the measurements similar to those of Fig. 6.4.

At first, it seemed that all of nature's forces were conspiring against us. Later we came to realize that it is our foolishness that we should blame, and that a low quality of electron-beam evaporated capping layers is to be expected. First, a constituent oxygen atom can be broken off both from aluminum oxide and silicone dioxide during the evaporation making these oxides a bad choice for the capping layer. Second, e-beam deposited oxides are expected to have a poor stoichiometry, and hence it is not surprising that a light oxygen molecule can diffuse through the resulting porous oxide film.

The problem of preventing oxidation of the electrodes turned out a hard nut to crack and to this day we have not found an adequate solution. Nevertheless,

we have some ideas of how to circumvent the problem; these ideas are discussed in the next two sections.

6.2 Electromigration after depositing the nanoparticles

As mentioned earlier, the permalloy electrodes used in the experiments of Chapters 4 and 5 were kept in ambient atmosphere before being measured and certainly have a surface layer of oxide on top of them. However, after electromigration the vast majority of our devices show no signatures of the asymmetry (Fig 6.3); the device resistance remains symmetric with respect to applied magnetic field when the field is large enough to saturate the magnetization. The reason for this is, we can guess, that the metal around the tunneling gap is unoxidized and only exposed from the bulk of the ferromagnet during the electromigration. The sample remains in cryogenic vacuum during both electromigration used to fabricate the device and the measurements, so that the device remains unoxidized during the experiment.

This suggests a possible modification of the approach used to fabricate the nanoparticle SET described in the third chapter: We can imagine first depositing the nanoparticles onto a ferromagnetic wire, cooling down the device, and then using the electromigration to both create source and drain electrodes and to electrostatically position the nanoparticle between the electrodes.

Our first attempts to fabricate test gold devices failed: during the electromigration the nanoparticles disappeared from the gap region (Fig. 6.5(a)), probably due to the enhanced surface diffusion at elevated temperatures associated with electromigration.

Since then, we have found out [1] that a presence of the molecular capping layer around the nanoparticle can prevent this "surface melting" and can allow

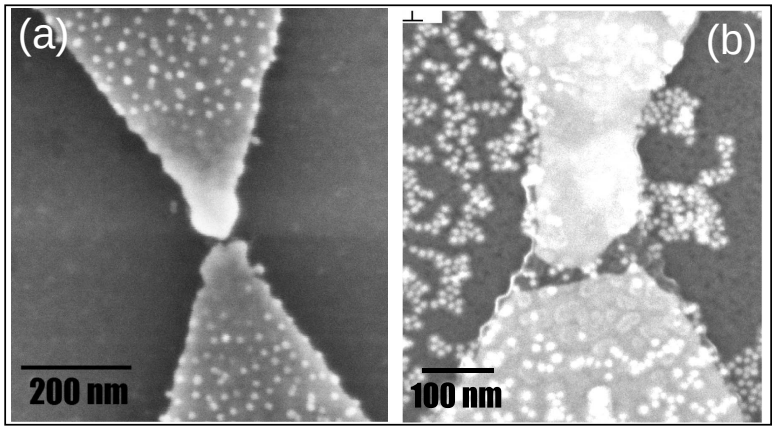


Figure 6.5: (a) Electromigration of gold electrodes after a self-assembled monolayer of gold nanoparticles was deposited. Notice the absence of the nanoparticles next to the gap between the electrodes. (b) Same as (a), except that before electromigration the SAM of nanoparticles was treated with ethanol solution of hexenedithiol. Note the particles in the gap region.

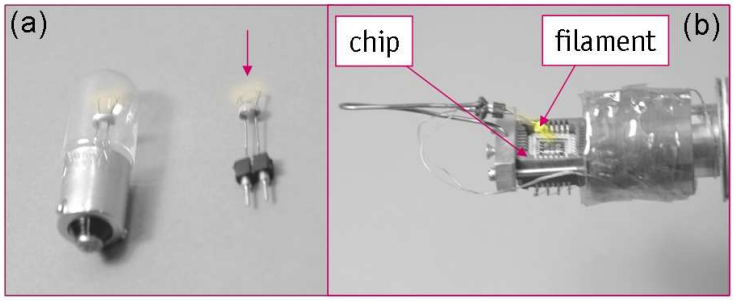


Figure 6.6: (a) A filament is extracted from a conventional lightbulb. (b) The filament is placed next to the chip on a helium dipstick.

some particles to survive electromigration and to be found inside the gap afterwards (Fig. 6.5(b)). A device with ferromagnetic electrodes might be fabricated following the same recipe adjusted for the change in chemistry at the self-assembly step. One can also imagine that performing electromigration may assist placing nanoparticles into the gap, analogous to the electrotrapping discussed in the Chapter 3.

6.3 Nanoparticle deposition inside the refrigerator

This idea builds on the nanoparticle SET fabrication technique described in the second chapter. There, we used an electron beam evaporator to deposit a sub-monolayer of metal, which in turn self-assembled into the particles. We would then break vacuum, unload the sample, load it into the refrigerator and cool it down to milliKelvin temperatures for measurements. As discussed earlier in this chapter, if the electrodes are ferromagnetic, oxidization occurs when the sample is transferred from the evaporator and to the refrigerator. To avoid this, we have designed a metal evaporator which can reside *inside* the refrigerator so that the SET is never exposed to oxygen during its fabrication.

The idea is very simple: we open a lightbulb (Fig. 6.6(a)), extract the filament and deposit a layer of metal (e.g. $\sim$ 200 nm of gold) on top of it inside a conventional e-beam evaporator. We mount the filament several millimeters away from the surface of the chip inside the dipstick (Fig. 6.6(b)) and connect the filament to an external voltage source. We then cool down the dipstick (creating a cryogenic vacuum) and apply a current of approximately 100 mA (Care needs to be taken not to damage the wiring of the dipstick). This is enough to heat up the filament to above the melting temperature of gold. Hence, metal is evaporated and nanoparticles are deposited while the chip is residing in a cryogenic vacuum inside the dipstick (Fig. 6.7(b)). After metal evaporation we found increased resistance and Coulomb blockade features (Fig. 6.7(a)) in the devices only exhibiting a slight tunneling current after electromigration. This serves as evidence for formation of nanoparticles bridging the tunneling gap. We have not so far cooled down any of these devices to milliKelvin temperatures in order to study the particle-in-a-box electron states. Nevertheless, we hope that in addition to preventing devices from oxidation, the technique may allow modifying the geometry of the "box" (the SET's island) while measuring particle-in-a-box states in-situ. This, in the author's opinion, makes the technique appealing enough to try as a high-risk big-prospects project.

6.4 SETs with ferromagnetic electrodes: theoretical proposals

We hope that one or several approaches mentioned above may result in a versatile fabrication technique for SETs with ferromagnetic electrodes. In this section we

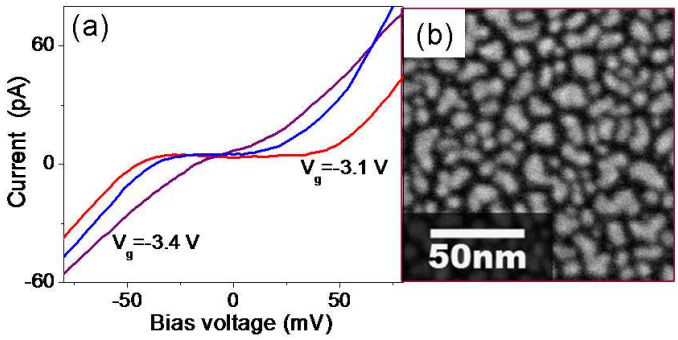


Figure 6.7: (a) After passing a current through the filament the metal deposited on the filament gets redeposited onto the surface of the chip (b) Some of the tunneling devices change their resistance and exhibit a Coulomb blockade after the evaporation.

discuss some of the theoretical proposals for probing the physics of single spins in such systems, mainly following the theoretical works of Braig *et al.* [8] and Martinek *et al.* [7]. We will briefly outline the results allowing experimental verification and refer the reader to the original work [16, 10] for the details.

The spin dependent transmission of the SET can be analyzed using either the rate equation approach for the density matrix of the system [8] or the non-equilibrium Green function method [7]. Even in the simplest regime of linear response ($eV < kT$), for a dot with a single level available, the spin accumulation significantly changes the conductance of such a spin-valve.

Martinek *et al.* [7] predict that in this regime the dependence of the conductance on the angle θ between the magnetization direction of the two electrodes differs significantly from the case of a spin-valve Eq. (1.14). Moreover, the angular dependence should acquire a dependance on the gate voltage (Fig. 6.8(c)). For a

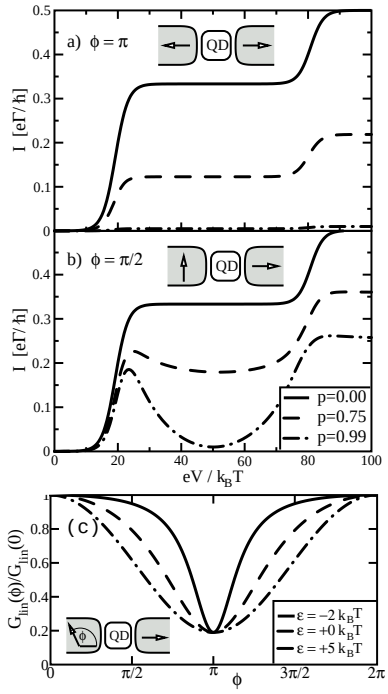


Figure 6.8: The results of Martinek et al. [7]. (Reproduced with permission from Jan Martinek.) (a), (b) Current across a ferromagnetic SET as a function of bias voltage in the non-linear regime, for different polarizations p of the electrons at the Fermi level. (a) Magnetization in the left and right electrode directed in the opposite directions ($\theta = 180°$). (b) $\theta = 90°$. (c) Differential conductance of the SET in the linear response regime $eV < kT$ as a function of angle between the magnetization direction of the two electrodes θ, for different gate voltages ϵ.

non-zero θ a non-trivial spin should be accumulated on the dot along the direction $\mathbf{M_L} - \mathbf{M_R}$.

In the non-linear regime ($eV > kT$) for a dot with one level available for tunneling, Martinek *et al.* predict a familiar-looking Coulomb blockade in the conductance as a function of the bias voltage (Fig. 6.8(a)). The transmission of the SET should be however suppressed for high spin polarization of the leads.

For $\theta = 90°$, spin accumulation should result in a negative differential conductance at high bias voltage (Fig. 6.8(b)). This would be a direct signature of the spin-accumulation on the island, and should be observed only for the electrodes with a high spin polarization p. The physics behind this effect is that the accumulated spin should precess in the exchange field (which vanishes at the point of current minimum in Fig. 6.8(b)), causing lifting of the "spin blockade" away from that point.

An externally applied magnetic field should cause a reduction of the accumulated spin due to its precession around the field direction. As a result, the differential conductance of the SET should acquire a clear magnetic field dependence (Fig 6.9). The width-at-half-maximum of the dip in Fig 6.9 would be related to the decoherence time of the spin on the island, making such a measurement a valuable tool for studying spin dynamics and decoherence.

For the more complicated case of a quantum dot with several levels available for tunneling, the presence of the ferromagnetic leads could reduce changes in the relative currents through each quantum level when comparing parallel and antiparallel configurations of the leads [10]. The conductance peak spectra may look very different for different magnetization orientations, both in term of the positions and the magnitudes of the most prominent peaks, leading to distinct

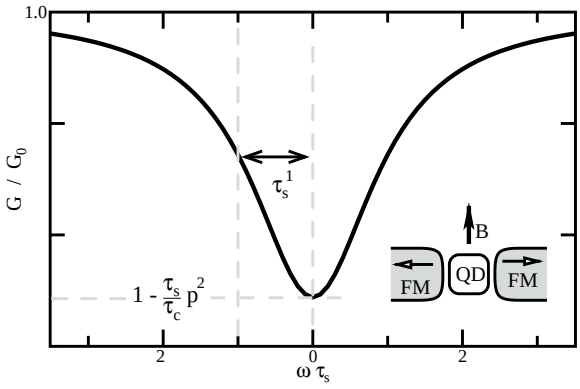


Figure 6.9: The results of Martinek et al. [16]. (Reproduced with permission from Jan Martinek). Differential conductance across the SET in the linear response regime as a function of applied magnetic field, with magnetization of the leads aligned antiparallel. The width at half-maximum of the resonance is inversely proportional to the spin-relaxation time.

experimental signatures.

6.5 More proposals for future experiments

In the end of this thesis we discuss some experimental proposals not involving spin injection into a SET. The few ideas that we mention are sorted by estimated complexity, from relatively easy to harder experiments.

One experiment that would require very little preparation is looking for the high-spin ground states of a platinum group metal nanoparticle. The intent for the experiment stems from theoretical work [4] predicting a continuous transition between a Fermi sea and ferromagnetically ordered ground states in case of a nanoscale object. Strong exchange interaction in small ferromagnets may result in a "partially ferromagnetic" ground state, i.e. the ground state with the spin different from the spin of a Fermi sea, 0 or $\frac{1}{2}$, depending on the parity of the electron

number. Due to its strong exchange interaction, palladium (or platinum, to a lesser degree) nanoparticles make perfect candidates for studying such higher-spin ground states. In a possible experiment, we can make use of the improved gating in our SETs and study the deviations from the spin-up-spin-down electron level filling as seen in gold nanoparticles (Chapter 2). Alternatively, we can examine the distribution of g-factors for the electron levels, g-factors higher than the free-space value of 2 are predicted [4]. On the experimental side, we have fabricated Pd and Pt nanoparticles capped with organic ligands and have seen them self-assemble onto the gold electrodes with high density (see Fig. 3.2,Chapter 3). The author expects that the last remaining step - wiring the nanoparticles to the electrodes should not be too different from the case of the gold nanoparticles. In particular, the electrotrapping technique discussed in the Chapter 3 may provide an easy wiring solution.

Similarly, improved gating may allow us to examine the structure of a ferromagnetic (or antiferromagnetic) ground state at the level of individual electron states. By comparing excitation spectra differing by one electron we may be able to extract detailed information about how the exchange interaction influences the interacting ground state. The main challenge for this experiment would be the synthesis of ferromagnetic (or antiferromagnetic) nanoparticles immune to oxidation. Although not easy, this should be possible (perhaps with little help from a chemist). For example, very monodisperse cobalt nanoparticles $2 - 11$ nm in size capped by organic ligands can be synthesized following Sun *et al.* [5]. Chromium nanoparticles my be obtained following Green *et al.* [6] or any other available recipe.

Provided that we can fabricate such ferromagnetic nanoparticle SETs, we can

envisage more elaborate experiments using high frequency measurements to probe the magnetization dynamics in ferromagnets. For example, spin relaxation in a ferromagnetic SET is predicted to depend on the gate voltage [3]; this may be probed by pulsed-gate techniques. Also, probing ferromagnetic resonance [2] on the level of individual spins may be an exciting goal.

Finally, we can imagine experiments probing the spin coherence and mesoscopic interference much more controllably than the experiments in Chapter 5 by synthesizing magnetic nanoparticles of a size comparable to the phase coherence length and establishing a good electrical contact to it. It would be interesting to observe the interference both in diffusive (scattering from impurities) and ballistic (scattering mainly from the boundary) ferromagnetic nanoparticles.

BIBLIOGRAPHY

[1] T. Taychatanapat, K. Bolotin, F. Kuemmeth, and D. C. Ralph, preparing for publication.

[2] J. C. Sankey, P. M. Braganca, A. G. F. Garcia, I. N. Krivorotov, R. A. Buhrman, D. C. Ralph, *cond-mat/0602105*.

[3] X. Waintal and P. W. Brouwer, *Phys. Rev. Lett.* **91**, 247201 (2003).

[4] P. W. Brouwer, Y. Oreg, and B. I. Halperin, *Phys. Rev. B* **60**, 13977 (1999).

[5] S. Sun and C. B. Murray, *J. Appl. Phys* **85**, 4325 (1999).

[6] M. Green and P. O'Brien, *Chem. Comm.*, 1912 (2001).

[7] J. Martinek, J. Barnas, S. Maekawa, H. Schoeller, and G. Schon, *Phys. Rev. B* **66**, 014402 (2002).

[8] S. Braig and P. W. Brouwer, *Phys. Rev. B* **71**, 195324 (2005).